

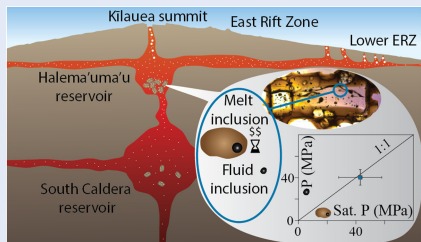
Reliability of Raman analyses of CO₂-rich fluid inclusions as a geobarometer at Kīlauea

C.L. DeVitre^{1*}  , P.E. Wieser¹

OPEN  ACCESS

<https://doi.org/10.7185/geochemlet.2404>

Abstract



Interpreting signals of volcanic unrest requires knowledge of the architecture of the magmatic system, particularly the depths at which magmas are stored. Such information can be vital to help predict changes in eruptive style and vigour. However, popular petrological tools to assess magma storage depths (*e.g.*, melt inclusions) are costly, present large uncertainties, and are too slow for real time monitoring. Here, we evaluate the reliability of Raman Spectroscopy measurements of CO₂-dominated fluid inclusions as a geobarometer relative to microthermometry and melt inclusion barometry. We calculate storage pressures for 102 olivine-hosted fluid inclusions from the 2018 Lower East Rift Zone eruption of Kīlauea, which are statistically indistinguishable to those determined from melt inclusions. We show that calibrated Raman spectroscopy yields densities within 5–10 % of microthermometry for CO₂-dominated fluid inclusions (<10 mol % H₂O) but is a far more suitable method for systems like Kīlauea dominated by shallow magma storage. Overall, pressures determined from fluid inclusions by Raman spectroscopy are robust and require only a fraction of the time and resources of melt inclusion studies.

Received 20 September 2023 | Accepted 19 December 2023 | Published 31 January 2024

Introduction

Understanding magma storage depth is crucial for interpreting volcanic signals, predicting eruptive changes and assessing the potential for volcanic unrest. This parameter is commonly determined using erupted materials and petrological tools like melt inclusion, mineral-mineral and mineral-melt barometry (Klügel *et al.*, 2005; Putirka, 2008; Barker *et al.*, 2021). However, many petrological tools present large uncertainties (*i.e.* ±8–19 km for clinopyroxene-based barometers; Wieser *et al.*, 2023) and require extensive sample preparation, making them unsuitable for real time monitoring. For example, melt inclusion work involves numerous time and resource consuming sample preparation, analytical and data processing steps (Fig. 1). Despite meticulous efforts, calculated pressures often come with significant analytical and systematic uncertainties (*e.g.*, melt and bubble volume measurements, solubility models, post-entrainment crystallisation corrections) that can range from 20 % to 50 % when fully propagated (Tucker *et al.*, 2019; Wieser *et al.*, 2021; DeVitre *et al.*, 2023).

CO₂-dominated fluid inclusions, tiny droplets of exsolved fluids enclosed in growing crystals within a degassing melt (Roedder, 1979), offer a compelling alternative to melt inclusions for deducing magma storage depths. At magmatic temperatures, the CO₂ density in a melt's exsolved fluid phase strongly depends on pressure, with little sensitivity to temperature (Dayton *et al.*, 2023). Therefore, with a well constrained CO₂ density within a fluid inclusion and a reasonable estimate of entrapment temperature, the entrapment pressure can be calculated using an equation of state (Fig. 1). Traditionally, CO₂

density in fluid inclusions has been assessed using microthermometry, which involves observing phase changes during heating and cooling. This method has proven successful in CO₂-dominated volcanic systems (<10 mol % H₂O), particularly those with deep magma storage systems like the Canary Islands, Cabo Verde Islands, and the Azores (Klügel *et al.*, 2005, 2020; Zanon and Frezzotti, 2013). However, it is difficult to measure fluid inclusions trapped in shallower volcanic systems (<~6 km) by microthermometry, because the density of CO₂ is below critical and the homogenisation of the liquid into the vapour phase is nearly impossible to observe optically (Hansteen and Klügel, 2008). Microthermometry also requires the use of specialised heating/cooling stages and the preparation of double polished crystal wafers (Fig. 1). The past decade of advances in the accuracy of Raman-based CO₂ densimetry has opened new avenues for the technique (Lamadrid *et al.*, 2017; DeVitre *et al.*, 2021). Specifically, Raman can measure the density of very small fluid inclusions (down to ~1 μm) and/or those with low bulk CO₂ densities (<0.45 g/cm³), impossible by microthermometry, with an accuracy of ~0.02 g/cm³ (Yuan and Mayanovic, 2017). Raman requires only a single polish to ensure visibility of fluid inclusions within ~50 μm of the surface, resulting in fewer preparation steps than microthermometry and melt inclusion work (Fig. 1). Because Raman is also commonly employed in fields like chemistry, biology, material science and physics, instrumentation is available at many research institutions. Recent studies suggest that fluid inclusions may have potential as a petrological monitoring tool, enabling relatively rapid constraints on magma storage depth (Dayton *et al.*, 2023).

1. University of California, Berkeley, Berkeley, CA 94270

* Corresponding author (email: cl.devitre@gmail.com)



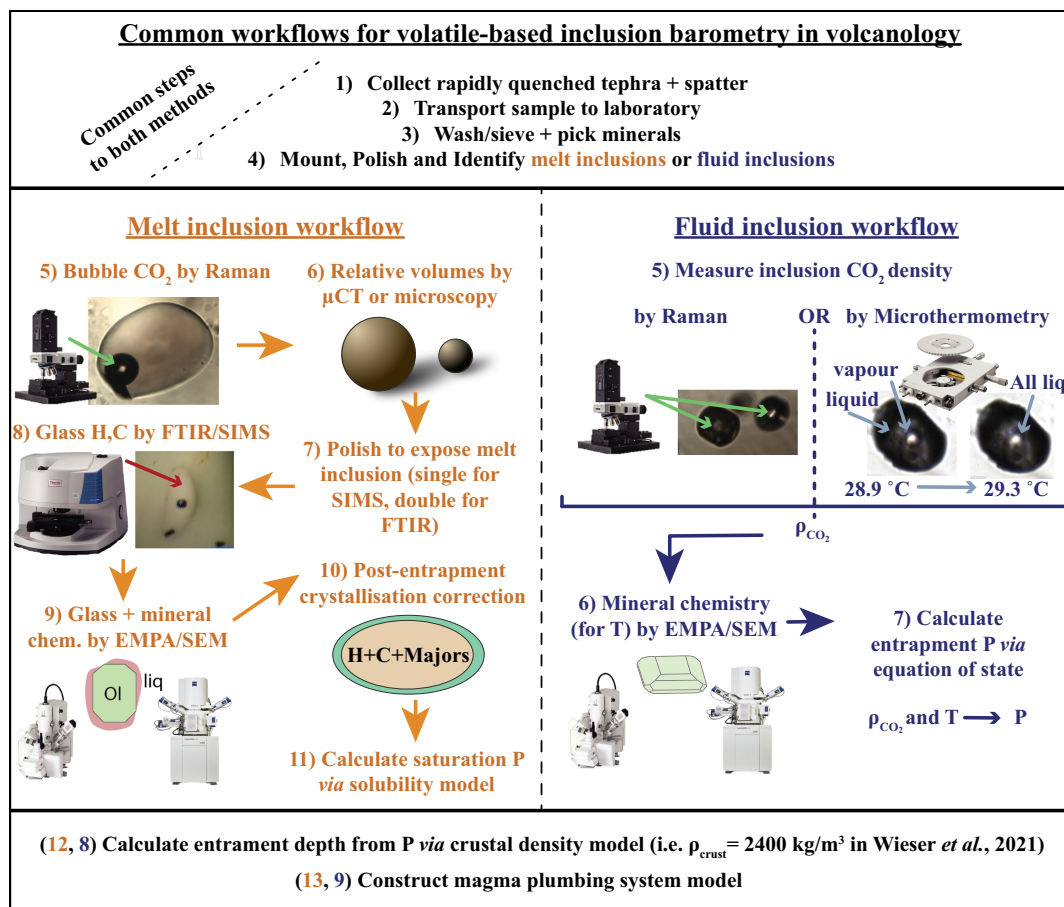


Figure 1 Melt inclusion and fluid inclusion workflows for magma storage depth measurements. Melt inclusion workflow steps are in orange text and fluid inclusion steps are in blue.

However, fluid inclusions are prone to post-entrapment modifications, like stretching and decrepitation, and significant re-equilibration before eruption (e.g., Wanamaker and Evans, 1989; Hansteen and Klügel, 2008). This rapid re-equilibration may cause fluid inclusions to reflect stalling levels rather than true capture depths (Hansteen and Klügel, 2008; Zanon and Frezzotti, 2013), or even undergo reset during slow quenching (Klügel *et al.*, 2020). As Raman-based fluid inclusion barometry gains popularity, a critical question arises: are the storage depths derived from CO₂-dominated fluid inclusions consistent with melt inclusion barometry and other estimates of magma storage depths, or are they consistently reset by late stage processes during magma ascent?

The 2018 Lower East Rift Zone (LERZ) eruption of Kīlauea volcano in Hawai'i is an ideal test bed to assess fluid inclusion barometry, given that this volcano is extremely well monitored, and geophysical methods have revealed two main regions of magma storage (1–2 km and ~3–5 km depth; Baker and Amelung, 2012; Anderson and Poland, 2016; Anderson *et al.*, 2019). These geophysical estimates were corroborated by melt inclusion work on erupted 2018 samples (Lerner *et al.*, 2021; Wieser *et al.*, 2021). However, it is notable that both melt inclusion studies were submitted ~2 years after the eruption had ended, a testament of the considerable analytical effort required (Fig. 1), and thus the unsuitability of this method as a monitoring tool. Here, we assess whether magma storage depths determined using Raman analyses of CO₂-dominated fluid inclusions would have yielded the same results. First, we evaluate the accuracy of the Raman method through a direct comparison with

microthermometry to validate our approach to determine entrapment pressures. We compare pressures from 102 olivine-hosted fluid inclusions to those of melt inclusions from the exact same samples (or crystals when possible). Our results reveal that magma storage depths calculated from fluid inclusion and melt inclusion barometry are statistically indistinguishable. However, fluid inclusions exhibit significantly smaller uncertainties and require far fewer preparation and analytical steps (Fig. 1).

Calibrated Raman Spectroscopy is a Suitable Alternative to Microthermometry

Despite its relative ease compared with microthermometry, and ability to assess a wider range of CO₂ densities, many aspects of the Raman method have been recently criticised (e.g., peak fitting, instrument drift, instrument calibrations), with suggestions it is “150× less accurate than microthermometry” (Bakker, 2021). To assess whether Raman spectroscopy can reliably be used to measure the density of CO₂-dominated fluid inclusions, we measured olivine-hosted fluid inclusions from Fogo volcano, Cabo Verde (DeVitre *et al.*, 2023) using both our calibrated Raman instrument and microthermometry ($\rho_{\text{CO}_2} > \sim 0.45 \text{ g/cm}^3$; Figs. 2a, S-4). We measured the inclusions on the Raman while maintaining a constant temperature of 37 °C and at low laser power to mitigate potential effects of laser induced heating on measured fermi diad separation (Hagiwara *et al.*, 2021). Melting

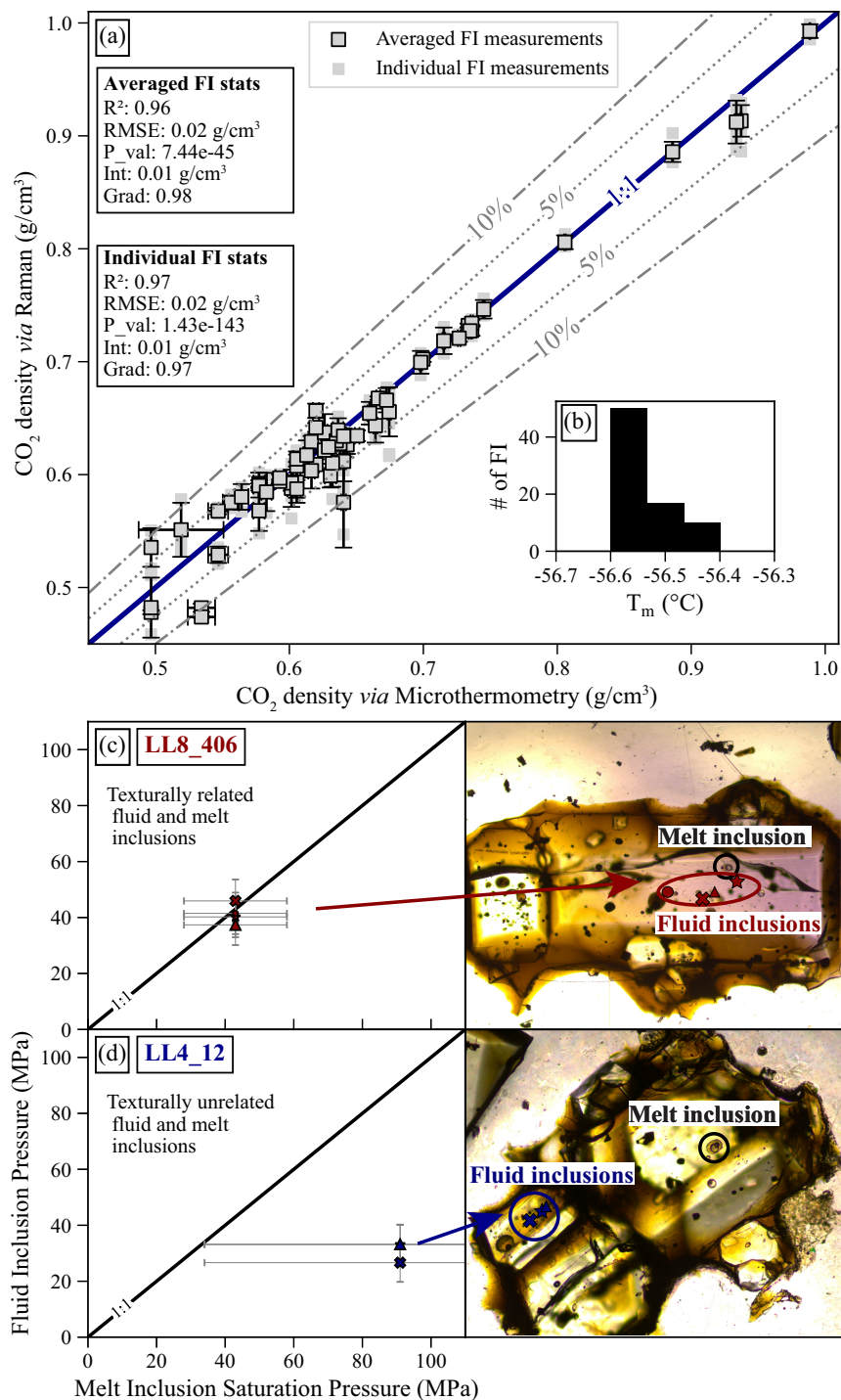


Figure 2 Comparison of Raman spectroscopy vs. Microthermometry, and of melt inclusion barometry vs. fluid inclusion barometry. **(a, b)** Density via Raman vs. density obtained from microthermometry. Outlined symbols represent averaged Raman measurement for each fluid inclusion and symbols without outlines are individual Raman measurements. Error bars show $\pm 1\sigma$ of repeated measurements for Raman and microthermometry. **(c)** Crystal with clearly texturally related melt inclusions and fluid inclusions (LL8_406) showing overlapping pressures. **(d)** Crystal with texturally unrelated melt inclusions and fluid inclusions (LL4_12); fluid inclusions are found in a smaller olivine crystal in the same crystal cluster and return lower pressures. Specific crystal plots and images for every other pair identified are provided in the [Supplementary Information Image Database](#) for detailed comparisons.

temperatures for all fluid inclusions analysed using microthermometry (11 crystals, ~60 fluid inclusions) are $-56.5 \pm 0.1 \text{ }^{\circ}\text{C}$ (Fig. 2a) which precludes the significant presence of any gaseous species other than CO_2 (confirmed via Raman Spectroscopy). Homogenisation temperatures obtained range from -11.1 ± 0.1 to $+31.6 \pm 1 \text{ }^{\circ}\text{C}$ (Fig. S-4b) and yield calculated bulk densities between 0.49 and 0.99 g/cm^3 (Fig. 2a). Results of

microthermometry and calibrated Raman spectroscopy are generally within 5 % of each other (Fig. 2a), and up to 10 % for inclusions with near critical CO_2 densities ($\sim 0.45 \text{ g}/\text{cm}^3$), where microthermometry becomes extremely sensitive to the accuracy of the homogenisation temperature and the phase transition is difficult to constrain (Hansteen and Klügel, 2008). Regression statistics confirm good agreement between the two methods

(Fig. 2a; $R^2 = 0.96$, RMSE = 0.02 g/cm³, $p = 7.44\text{e-}45$). Overall, this comparison validates Raman spectroscopy measurements as a suitable alternative to microthermometric measurements (see also Kobayashi *et al.*, 2012).

Fluid and Melt Inclusion Pressures Yield a Consistent Petrogenetic Model

Having validated the Raman method for CO₂ density measurements, we aim to assess whether fluid inclusion pressures are a viable alternative to the commonly used melt inclusion method. The most robust comparison involves examining pressures from melt and fluid inclusions within a single crystal. Accordingly, we analysed 36 CO₂-dominated fluid inclusions in 17 crystals that also contained melt inclusions, as measured by Wieser *et al.* (2021; Fig. 2). Petrographic analysis was conducted to categorise fluid inclusions based on their shapes, positions, and approximate textural relationship to the melt inclusions. We remove fluid inclusions with a significant melt film (>20 vol. %) and poor quality Raman analyses (see *Supplementary Information*). Overall, we find that fluid inclusions hosted in the same crystals, same inclusion assemblages or apparent growth zones record the same entrapment pressures as reconstructed melt inclusions within the uncertainty of the methods (Fig. 2b). In contrast, texturally unrelated fluid inclusions and melt inclusions (*e.g.*, the fluid inclusion is present in the same crystal cluster but within a separate smaller crystal) tend to yield different pressures (Fig. 2d). If crystals were attached *via* synneusis (Wieser *et al.*, 2019; DiBenedetto *et al.*, 2020), it is very plausible that the smaller crystal grew in a different environment, explaining the lower fluid inclusion pressure (Fig. 2c). In general, it appears that if fluid inclusions are well documented and selected with care (*i.e.* fluid inclusions in crystal core growth zones), the estimates of pressure for fluid inclusions are consistent with those from melt inclusion work at Kilauea.

The large errors on melt inclusion pressures are notable during these comparisons and mainly result from uncertainty in the relative volume of the vapour bubble (orange 'MI w/VB' error bar in Fig. 3; Wieser *et al.*, 2021; Tucker *et al.*, 2019). The uncertainties on CO₂-dominated fluid inclusion pressures are much smaller as they are only a result of peak fitting, drift corrections, and uncertainty in the temperature of fluid trapping/re-equilibration (Wieser and DeVitre, 2023). These sources of uncertainty were propagated in DiadFit (Wieser and DeVitre, 2013) using Monte Carlo simulations considering 50 K uncertainty on the temperature (see *Supplementary Information* for details on temperature) and a 1 σ uncertainty on density based on peak fit uncertainties of CO₂ spectra as well as the uncertainty in the Ne correction model. We also correct pressures for the presence of H₂O in the exsolved fluid using the mixed CO₂-H₂O EOS of Duan and Zhang (2006) using $X_{\text{H}_2\text{O}}$ values inferred from melt inclusion data at Kilauea (Wieser *et al.*, 2021), further propagating the additional uncertainty introduced by this correction step (see Section S-3 of the *Supplementary Information*).

Due to the scarcity of fluid inclusions in the exact same crystal as melt inclusions, direct comparisons are limited. To complement our dataset, we also analysed an additional 109 fluid inclusions in olivine crystals picked directly from the same sample split as the melt inclusions. After filtering those with >20 % melt film and poor quality spectra, we report a total of 102 fluid inclusions and compare them with 103 melt inclusions from Wieser *et al.* (2021). When subdivided by sample (May, July, August 2018), histograms indicate good agreement between the pressures recorded by fluid inclusions and melt

inclusions (Fig. 3a-c), particularly when considering the analytical uncertainty associated with melt inclusions measurements.

We apply the Kolmogorov–Smirnov test (KS) to evaluate if observed visual differences are statistically significant. Sample KS tests reveal that melt and fluid inclusion pressures are not significantly different for May 2018 ($p = 0.16$) but suggest a possible significant difference for July and August 2018 ($p = 0.001$ and 0.03, respectively). However, these comparisons are constrained by the relatively small n for each sample ($n < 50$) and the comparatively large analytical errors on melt inclusion measurements. To address this limitation, we conduct a Monte Carlo simulation using Python3, re-sampling each melt and fluid inclusion measurement 1000 times within analytical uncertainty. KS tests on these re-sampled distributions indicate that the fluid and melt inclusion pressure distributions are not significantly different for any of the three events ($p = 0.44 \pm 0.20$, 0.05 ± 0.05 and 0.02 ± 0.03 for May, July and August, respectively), with differences attributable to the uncertainty in melt inclusion measurements.

Until now, we focused on the analytical uncertainty tied to melt and fluid inclusion saturation pressures. However, reconstructed melt inclusion H₂O and CO₂ concentrations undergo conversion into pressures using a solubility model, introducing substantial systematic uncertainty (see Wieser *et al.*, 2022). In Figure 3g-i, we present pressures calculated using the MagmaSat model (Ghiorso and Gualda, 2015), deemed most suitably calibrated at Kilauea by Wieser *et al.* (2021). Yet, little consensus exists; for the same eruption, Lerner *et al.* (2021) employed the solubility model of Iacono-Marziano *et al.* (2012). Cumulative melt inclusion pressures for five different solubility models indicate that the uncertainty linked to model choice can readily explain any slight differences between melt and fluid inclusion pressures (Fig. S-9). Another advantage of fluid inclusion barometry, compared to melt inclusion barometry, is that the choice of EOS does not significantly contribute to the uncertainty (Hansteen and Klügel, 2008).

Slight differences between fluid and melt inclusion pressures may be attributed to sampling bias linked to the complex histories of the 2018 crystal cargo. Lerner *et al.* (2021) and Wieser *et al.* (2021) proposed that crystals originate from two storage reservoirs beneath Kilauea's summit based on the relationship between melt inclusion saturation pressures, entrapment depths, and olivine forsterite content (Fo = Mg²⁺ / [Mg²⁺ + Fe²⁺], atomic). Specifically, Wieser *et al.* (2021) reported entrapment depths of 0.89–1.74 km for low Fo (<81.5 mol %) olivines in equilibrium with the carrier melt and ~2–5 km for high Fo (>81.5 mol %) olivines, aligning with geophysical estimates for the two magma reservoirs at Kilauea (Poland *et al.*, 2014; Anderson *et al.*, 2019). Fluid inclusion pressures support this correlation, with those trapped in lower Fo content olivine crystals tending to have lower entrapment pressures (Fig. 3g-i). This highlights that similar petrogenetic interpretations can be derived from both fluid and melt inclusions.

Assessing Fluid Inclusion Re-equilibration

Although differences between melt inclusions and fluid inclusions are not statistically significant (Fig. 3d-f), some fluid inclusions indicate shallower pressures compared to melt inclusions for an equivalent olivine Fo content (*i.e.*, Fig. 3e,h). Unlike melt inclusions, which contend with significant systematic uncertainties related to solubility models (Fig. S-9), the primary source of uncertainty for CO₂-dominated fluid inclusions is re-equilibration during prolonged storage and transport. To assess whether re-equilibration could explain the seemingly lower



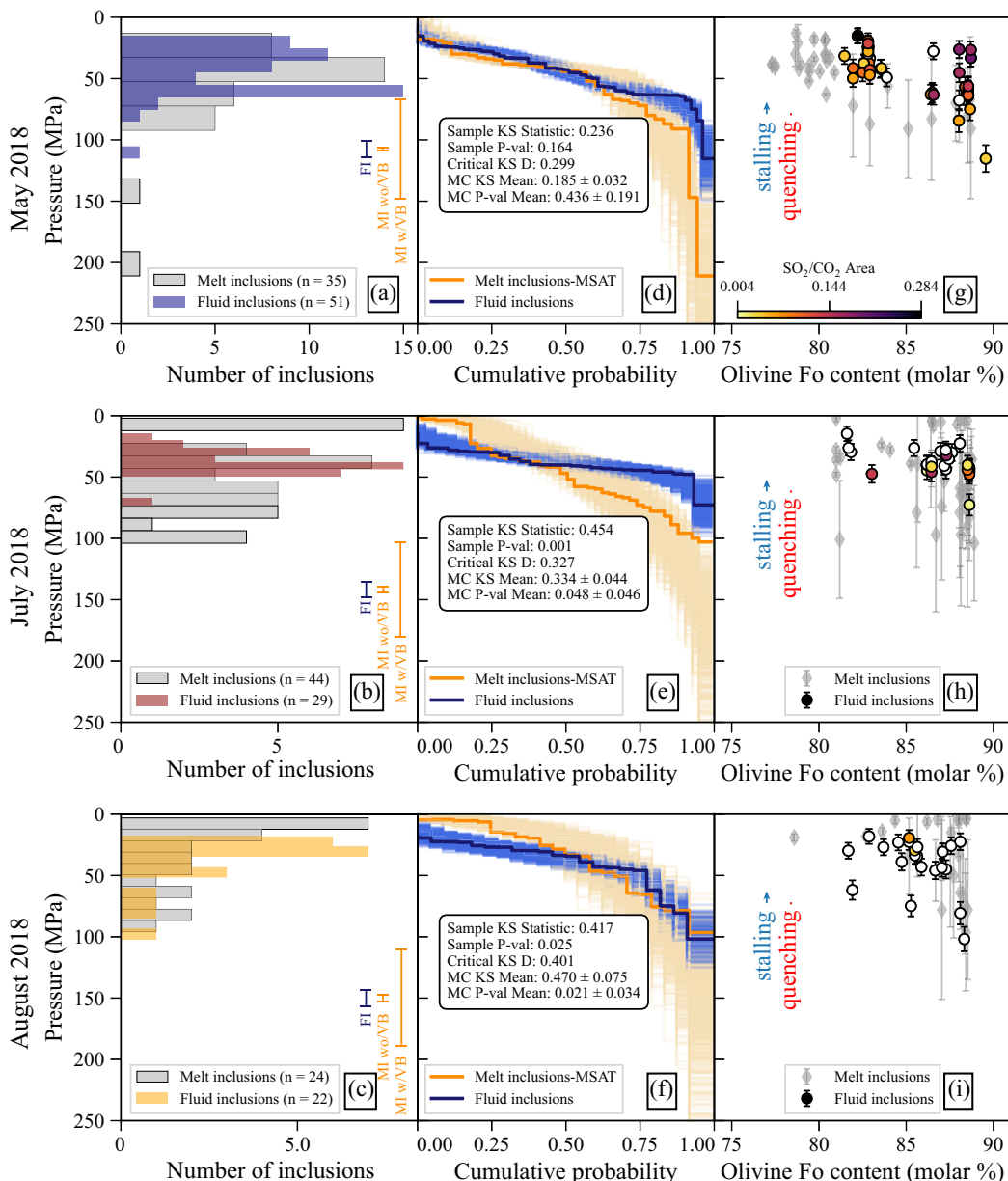


Figure 3 Comparing fluid inclusion and melt inclusion pressures for May, July and August 2018. (a–c) Histograms of pressures, with error bars indicate the average 1σ uncertainty for melt inclusions with vapour bubbles (MI w/VB) and without vapour bubbles (MI wo/VB), and the average 1σ fluid inclusion (FI) uncertainty. (d–f) Results of KS tests comparing fluid inclusion and melt inclusion pressure cumulative probability functions (CDF) from Monte Carlo simulations. For melt inclusions, the MagmaSat (Ghiorso and Gualda, 2015) results are shown (further details and five different solubility models in [Supplementary Information](#)). (g–i) Melt inclusion and fluid inclusion pressures vs. Fo content of the host olivine for (g) May 2018, (h) July 2018 and (i) August 2018. Fluid inclusions are coloured by SO_2/CO_2 peak area ratio. Blue and red arrows depict the maximum reduction in the internal pressure of a fluid inclusion trapped at the South Caldera reservoir induced by slow quenching (red in [Fig. 4a, b](#)) and 2 year stalling (blue in [Fig. 4c, d](#)).

pressures recorded by fluid inclusions in July 2018, we constructed a Python3 implementation of the mechanical re-equilibration model of Wanamaker and Evans (1989) based on olivine relaxation through dislocation creep (RelaxiFI; see [Data Availability](#)). We model the effect of fluid inclusion stretching on the internal pressure and CO_2 density for fluid inclusions using the EOS of Span and Wagner (1996). We consider fluid inclusions with a radius of 1 and 20 μm at variable distances (50–500 μm) from crystal defect structures (*i.e.* cracks, crystal edges and boundaries). It has also been suggested that fluid inclusions erupted in lava flows may re-equilibrate during post-eruptive cooling (Klügel *et al.*, 2020). The May 2018 sample is a rapidly quenched reticulite, and the Aug 2018 sample was water quenched from the lava channel. In contrast, the July

2018 sample was an air cooled overflow from the channel. Based on observing the formation and quenching of other overflows, we predict that cooling occurred within hours. However, even allowing up to 7 days of re-equilibration results in less than 1 % difference ([Fig. 4a, b](#)), well within analytical uncertainty. Next, we consider a fluid inclusion which may have been trapped in the deeper South Caldera reservoir (~ 4 km, 1300 °C) before being mobilised to the Halema'uma'u reservoir (~ 1 km depth, 1150 °C), and stored for 0–2 years prior to eruption (based on diffusion timescales from Mourey *et al.*, 2023; [Fig. 4c, d](#)). In the most extreme case (stretching of a 20 μm radius fluid inclusion found 50 μm from a crystal defect), stalling for 2 years causes a decrease in CO_2 density of less than 10 %, also smaller than the average measurement uncertainty.

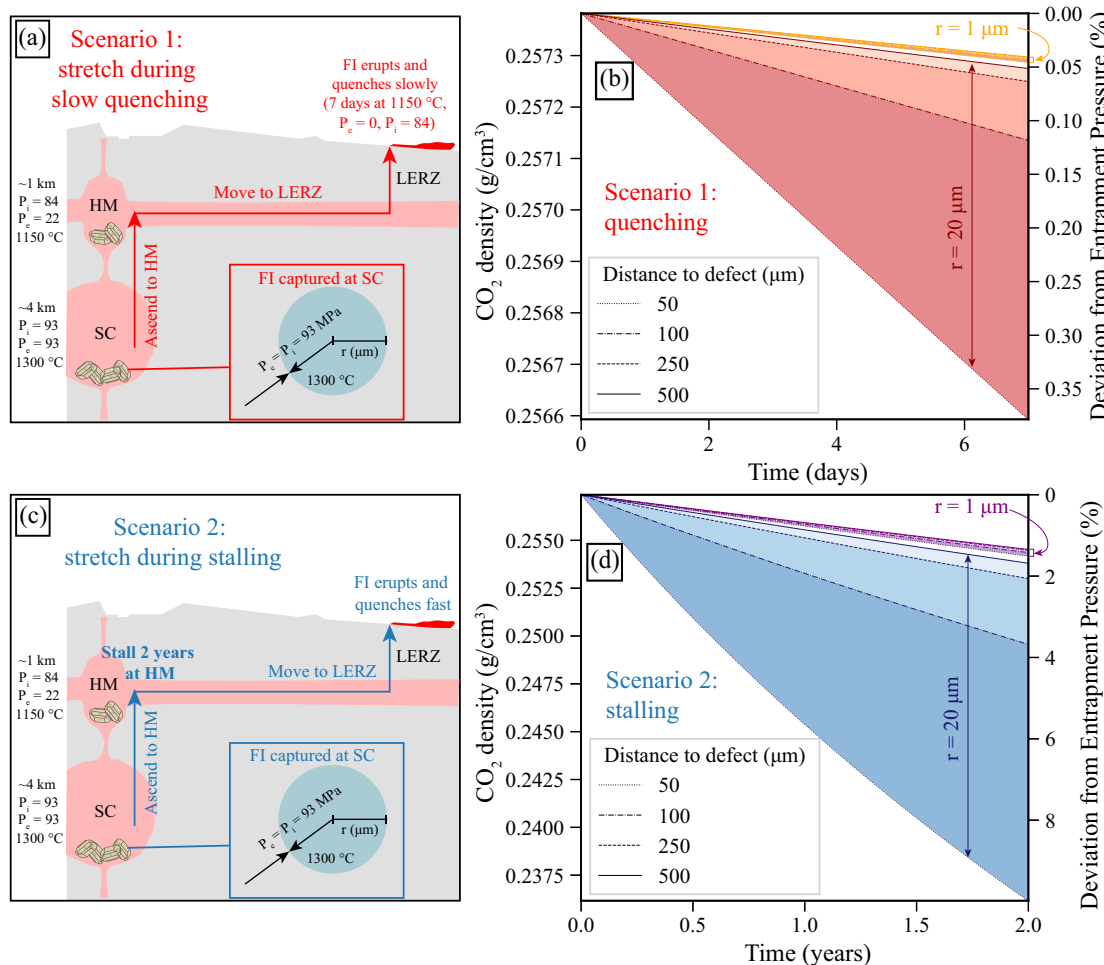


Figure 4 Assessing crystal cargoes and fluid inclusion re-equilibration. (a) Schematic diagram of Kilauea plumbing system showing the scenario modelled in (b), where 1 and 20 μm radii fluid inclusions are captured in olivine crystals at the South Caldera (SC), they are transported to Halema'uma'u (HM) reservoir, almost immediately mobilised to the Lower East Rift Zone (LERZ), erupted, and slowly quenched for 7 days (T is kept at 1150°C in the model). (b) Stretching model for slow quenching scenario in (a). (c) Diagram for the scenario modelled in (d), where the magma stalls at Halema'uma'u (HM) reservoir for 2 years prior to eruption. (d) Stretching model for stalling scenario in (c).

Overall, our results indicate that in shallow systems such as that of Kilauea where the internal pressure of the fluid inclusion is relatively low, stretching on timescales relevant to magma storage in upper storage reservoirs and syn-eruptive quenching is unlikely to play a major role and re-equilibration is of no significant concern.

Conclusions

In analysing the 2018 LERZ eruption of Kilauea volcano, we compared magma storage depth estimates using CO_2 -dominated fluid inclusions to those obtained through melt inclusion studies. Our findings suggest that fluid inclusions at Kilauea are minimally affected by re-equilibration within relevant timescales for magma storage and migration. They consistently reflect entrapment depths comparable to melt inclusions in the same samples. Consequently, fluid inclusions emerge as a reliable alternative to melt inclusions for barometry in shallow CO_2 -dominated volcanic systems.

Author Contributions

CLD prepared the Fogo fluid inclusions, performed all Raman and microthermometry analyses, developed the MC subsampling and fluid inclusion re-equilibration code, and wrote the manuscript.

PEW acquired the funding, prepared the Kilauea fluid inclusions, wrote the peak fitting/EOS code, and edited the manuscript.

Acknowledgements

PEW and CLD acknowledge support from NSF EAR 2217371 and the Berkeley Rose Hills Innovator Program. We thank Dale Burns at Stanford University for assistance with the EMPA measurements. We thank Ricardo S. Ramalho for collecting the Fogo volcano samples. This work was possible thanks to the fabulous samples collected by USGS field teams in 2018 and we are particularly grateful of Frank Trusdell's help with lava sampling as part of the PlumeTeam 2018 aerosol campaign. We also thank two anonymous reviewers and the editor Raúl Fonseca for their constructive comments which helped improve this manuscript.

Editor: Raul O.C. Fonseca

Data Availability

All data are made available with the publication. All data are also available on Github (<https://github.com/cljdevitre/KilaueaMIFI2023>) along with notebooks to reproduce figures

published in the article, the notebooks for running the MC KS test simulations and data processing notebooks. This repository is archived on Zenodo (<https://zenodo.org/doi/10.5281/zenodo.10520936>). Peak fitting and EOS calculations were performed in DiadFit (see <https://github.com/PennyWieser/DiadFit>, <https://doi.org/10.31223/X5CQ1F>). The python3 tool developed to assess re-equilibration of FI is available at <https://github.com/cljdevitre/RelaxiFI>.

Additional Information

Supplementary Information accompanies this letter at <https://www.geochemicalperspectivesletters.org/article/2404>.



© 2024 The Authors. This work is distributed under the Creative Commons Attribution 4.0 License, which permits unrestricted use, distribution, and reproduction in any medium, provided the original author and source are credited. Additional information is available at <http://www.geochemicalperspectivesletters.org/copyright-and-permissions>.

Cite this letter as: DeVitre, C.L., Wieser, P.E. (2024) Reliability of Raman analyses of CO₂-rich fluid inclusions as a geobarometer at Kilauea. *Geochim. Persp. Let.* 29, 1–8. <https://doi.org/10.7185/geochemlet.2404>

References

ANDERSON, K.R., POLAND, M.P. (2016) Bayesian estimation of magma supply, storage, and eruption rates using a multiphysical volcano model: Kilauea Volcano, 2000–2012. *Earth and Planetary Science Letters* 447, 161–171. <https://doi.org/10.1016/j.epsl.2016.04.029>

ANDERSON, K.R., JOHANSON, I.A., PATRICK, M.R., GU, M., SEGALL, P., POLAND, M.P., MONTGOMERY-BROWN, E.K., MIKLIUS, A. (2019) Magma reservoir failure and the onset of caldera collapse at Kilauea Volcano in 2018. *Science* 366, eaaz1822. <https://doi.org/10.1126/science.aaz1822>

BAKER, S., AMELUNG, F. (2012) Top-down inflation and deflation at the summit of Kilauea Volcano, Hawai'i observed with InSAR. *Journal of Geophysical Research: Solid Earth* 117, B12406. <https://doi.org/10.1029/2011JB009123>

BAKKER, R.J. (2021) The perfection of Raman spectroscopic gas densimeters. *Journal of Raman Spectroscopy* 52, 1923–1948. <https://doi.org/10.1002/jrs.6245>

BARKER, A.K., RYDEBLAD, E.M., SILVA, S.M.D.M. (2021) Magma Storage at Ocean Islands: Insights From Cape Verde. In: MASOTTA, M., BEIER, C., MOLLO, S. (Eds.) *Crustal Magmatic System Evolution: Anatomy, Architecture, and Physico-Chemical Processes*. American Geophysical Union and Wiley, Hoboken, NJ, 45–78. <https://doi.org/10.1002/9781119564485.ch3>

DAYTON, K., GAZEL, E., WIESER, P., TROLL, V.R., CARRACEDO, J.C., LA MADRID, H., ROMAN, D.C., WARD, J., AULINAS, M., GEIGER, H., DEEGAN, F.M., GIBERT, G., PEREZ-TORRADO, F.J. (2023) Deep magma storage during the 2021 La Palma eruption. *Science Advances* 9, eade7641. <https://doi.org/10.1126/sciadv.ade7641>

DEVITRE, C.L., ALLISON, C.M., GAZEL, E. (2021) A high-precision CO₂ densimeter for Raman spectroscopy using a Fluid Density Calibration Apparatus. *Chemical Geology* 584, 120522. <https://doi.org/10.1016/j.chemgeo.2021.120522>

DEVITRE, C.L., GAZEL, E., RAMALHO, R.S., VENUGOPAL, S., STEELE-MACINNIS, M., HUA, J., ALLISON, C.M., MOORE, L.R., CARRACEDO, J.C., MONTELEONE, B. (2023) Oceanic intraplate explosive eruptions fed directly from the mantle. *Proceedings of the National Academy of Sciences* 120, e2302093120. <https://doi.org/10.1073/pnas.2302093120>

DI BENEDETTO, M., QIN, Z., STUCKALE, J. (2020) Crystal aggregates record the pre-eruptive flow field in the volcanic conduit at Kilauea, Hawaii. *Science Advances* 6, eabd4850. <https://doi.org/10.1126/sciadv.abd4850>

DUAN, Z., ZHANG, Z. (2006) Equation of state of the H₂O, CO₂, and H₂O–CO₂ systems up to 10 GPa and 2573.15 K: Molecular dynamics simulations with ab initio potential surface. *Geochimica et Cosmochimica Acta* 70, 2311–2324. <https://doi.org/10.1016/j.gca.2006.02.009>

GHIORSO, M.S., GUALDA, G.A.R. (2015) An H₂O–CO₂ mixed fluid saturation model compatible with rhyolite-MELTS. *Contributions to Mineralogy and Petrology* 169, 53. <https://doi.org/10.1007/s00410-015-1141-8>

HAGIWARA, Y., YOSHIDA, K., YONEDA, A., TORIMOTO, J., YAMAMOTO, J. (2021) Experimental variable effects on laser heating of inclusions during Raman spectroscopic analysis. *Chemical Geology* 559, 119928. <https://doi.org/10.1016/j.chemgeo.2020.119928>

HANSTEEN, T.H., KLÜGEL, A. (2008) Fluid Inclusion Thermobarometry as a Tracer for Magmatic Processes. *Reviews in Mineralogy and Geochemistry* 69, 143–177. <https://doi.org/10.2138/rmg.2008.69.5>

IACONO-MARZIANO, G., MORIZET, Y., LE TRONG, E., GAILLARD, F. (2012) New experimental data and semi-empirical parameterization of H₂O–CO₂ solubility in mafic melts. *Geochimica et Cosmochimica Acta* 97, 1–23. <https://doi.org/10.1016/j.gca.2012.08.035>

KOBAYASHI, T., YAMAMOTO, J., HIRAJIMA, T., ISHIBASHI, H., HIRANO, N., LAI, Y., PRIKHOD'KO, V.S., ARAI, S. (2012) Conformity and precision of CO₂ densimetry in CO₂ inclusions: microthermometry versus Raman microspectroscopic densimetry. *Journal of Raman Spectroscopy* 43, 1126–1133. <https://doi.org/10.1002/jrs.3134>

KLÜGEL, A., HANSTEEN, T.H., GALIPP, K. (2005) Magma storage and underplating beneath Cumbre Vieja volcano, La Palma (Canary Islands). *Earth and Planetary Science Letters* 236, 211–226. <https://doi.org/10.1016/j.epsl.2005.04.006>

KLÜGEL, A., DAY, S., SCHMID, M., FARIA, B. (2020) Magma Plumbing During the 2014–2015 Eruption of Fogo (Cape Verde Islands). *Frontiers in Earth Science* 8, 157. <https://doi.org/10.3389/feart.2020.00157>

LAMADRID, H.M., MOORE, L.R., MONCADA, D., RIMSTIDT, J.D., BURRUSS, R.C., BODNAR, R.J. (2017) Reassessment of the Raman CO₂ densimeter. *Chemical Geology* 450, 210–222. <https://doi.org/10.1016/j.chemgeo.2016.12.034>

LERNER, A.H., WALLACE, P.J., SHEA, T., MOUREY, A.J., KELLY, P.J., NADEAU, P.A., ELIAS, T., KERN, C., CLOR, L.E., GANSECKI, C., LEE, R.L., MOORE, L.R., WERNER, C.A. (2021) The petrologic and degassing behavior of sulfur and other magmatic volatiles from the 2018 eruption of Kilauea, Hawai'i: melt concentrations, magma storage depths, and magma recycling. *Bulletin of Volcanology* 83, 43. <https://doi.org/10.1007/s00445-021-01459-y>

MOUREY, A.J., SHEA, T., COSTA, F., SHIRO, B., LONGMAN, R.J. (2023) Years of magma intrusion primed Kilauea Volcano (Hawai'i) for the 2018 eruption: evidence from olivine diffusion chronometry and monitoring data. *Bulletin of Volcanology* 85, 18. <https://doi.org/10.1007/s00445-023-01633-4>

POLAND, M.P., MIKLIUS, A., MONTGOMERY-BROWN, E.K. (2014) Magma supply, storage, and transport at shield-stage Hawaiian volcanoes. In: POLAND, M.P., TAKAHASHI, T.J., LANDOWSKI, C.M. (Eds.) *Characteristics of Hawaiian Volcanoes*, USGS Professional Paper 1801. US Geological Survey, Reston, VA, 179–234. <https://doi.org/10.3133/pp18015>

PUTIRKA, K.D. (2008) Thermometers and Barometers for Volcanic Systems. *Reviews in Mineralogy and Geochemistry* 69, 61–120. <https://doi.org/10.2138/rmg.2008.69.3>

ROEDDER, E. (1979) Origin and significance of magmatic inclusions. *Bulletin de Minéralogie* 102, 487–510. <https://doi.org/10.3406/bulmi.1979.7299>

SPAN, R., WAGNER, W. (1996) A New Equation of State for Carbon Dioxide Covering the Fluid Region from the Triple-Point Temperature to 1100 K at Pressures up to 800 MPa. *Journal of Physical and Chemical Reference Data* 25, 1509–1596. <https://doi.org/10.1063/1.555991>

TUCKER, J.M., HAURI, E.H., PIETRUSZKA, A.J., GARCIA, M.O., MARSKE, J.P., TRUSSELL, F.A. (2019) A high carbon content of the Hawaiian mantle from olivine-hosted melt inclusions. *Geochimica et Cosmochimica Acta* 254, 156–172. <https://doi.org/10.1016/j.gca.2019.04.001>

WANAMAKER, B.J., EVANS, B. (1989) Mechanical re-equilibration of fluid inclusions in San Carlos olivine by power-law creep. *Contributions to Mineralogy and Petrology* 102, 102–111. <https://doi.org/10.1007/BF01160194>

WIESER, P.E., DEVITRE, C.L. (2023) DiadFit: An Open-Source Python3 Tool for Peak fitting of Raman Data from silicate melts and CO₂ fluids. *EarthArXiv* Preprint v3. <https://doi.org/10.31223/X5CQ1F>

WIESER, P.E., VUKMANOVIC, Z., KILIAN, R., RINGE, E., HOLNESS, M.B., MACLENNAN, J., EDMONDS, M. (2019) To sink, swim, twin, or nucleate: A critical appraisal of crystal aggregation processes. *Geology* 47, 948–952. <https://doi.org/10.1130/G46660.1>

WIESER, P.E., LAMADRID, H., MACLENNAN, J., EDMONDS, M., MATTHEWS, S., IACOVINO, K., JENNER, F.E., GANSECKI, C., TRUSSELL, F., LEE, R.L., ILYINSKAYA, E. (2021) Reconstructing Magma Storage Depths for the 2018 Kilauean Eruption From Melt Inclusion CO₂ Contents: The Importance of Vapor Bubbles. *Geochemistry, Geophysics, Geosystems* 22, e2020GC009364. <https://doi.org/10.1029/2020GC009364>

WIESER, P.E., IACOVINO, K., MATTHEWS, S., MOORE, G., ALLISON, C.M. (2022) VESical: 2. A Critical Approach to Volatile Solubility Modeling Using an



Open-Source Python3 Engine. *Earth and Space Science* 9, e2021EA001932. <https://doi.org/10.1029/2021EA001932>

WIESER, P.E., KENT, A.J.R., TILL, C.B., DONOVAN, J., NEAVE, D.A., BLATTER, D.L., KRAWCZYNKI, M.J. (2023) Barometers Behaving Badly I: Assessing the Influence of Analytical and Experimental Uncertainty on Clinopyroxene Thermobarometry Calculations at Crustal Conditions. *Journal of Petrology* 64, egac126. <https://doi.org/10.1093/petrology/egac126>

YUAN, X., MAYANOVIC, R.A. (2017) An Empirical Study on Raman Peak Fitting and Its Application to Raman Quantitative Research. *Applied Spectroscopy* 71, 2325–2338. <https://doi.org/10.1177/0003702817721527>

ZANON, V., FREZZOTTI, M.L. (2013) Magma storage and ascent conditions beneath Pico and Faial islands (Azores archipelago): A study on fluid inclusions. *Geochemistry, Geophysics, Geosystems* 14, 3494–3514. <https://doi.org/10.1002/ggge.20221>

Reliability of Raman analyses of CO₂-rich fluid inclusions as a geobarometer at Kīlauea

C.L. DeVitre, P.E. Wieser

Supplementary Information

The Supplementary Information includes:

- 1. Detailed Materials and Methods
- 2. Statistical Significance of the MI vs. FI Recorded Pressures
- 3. Fluid % Effect on Calculated Densities and Pressures
- Figures S-1 to S-13
- Tables S-1 to S-7
- Supplementary Image Database
- Supplementary Information References

All raw data, including spectra, fitting images and Jupyter Lab notebooks to process and plot data can be found on the Github repository <https://github.com/cljdevitre/KilaueaMIFI2023>, which is archived on Zenodo (<https://zenodo.org/doi/10.5281/zenodo.10520936>).

1. Detailed Materials and Methods

1.1 Samples

Olivines from three samples of the 2018 LERZ eruption of Kīlauea volcano in Hawai‘i (Fissure 8 samples of May, July and August 2018) were picked under a binocular microscope, and individually mounted in CrystalBond™ on glass slides from jaw crushed and sieved samples as described in Wieser *et al.* (2021). The May 2018 sample erupted on 30 May 2018 (Lab code LL4, USGS code KE62–3293), as vesicular reticulite and scoria; The July 2018 sample erupted in mid-July, 2018 (Lab code LL8, no USGS code) was sampled from the selvages of a naturally quenched, and highly vesicular proximal overflow from the Fissure 8 channel; The August 2018 sample erupted on 1 August 2018 (Lab code LL7, USGS code KE62–A3321F) and was sampled directly from the channel and rapidly quenched in water (Wieser *et al.*, 2021). FI were revealed by grinding using 250–3000 grade wet and dry paper. Petrographic work was done to describe the emplacement of FI and FIA in the crystals. Photos were taken of the crystals and FI (see SI Image Database). Additionally, FI were located and photographed in the same crystals as those in which melt inclusions were analysed in Wieser *et al.* (2021). In total we analysed 145 FI hosted in 57 olivine crystals from the 2018 LERZ eruption of Kīlauea volcano. In the final dataset (102 fluid inclusions), we discarded spectra that yielded density errors



>20 % due to poor spectral quality (*e.g.*, high and/or wavy backgrounds, low signal/noise ratio) and excluded fluid inclusions with a melt film that occupied more than 20 % of the inclusion volume.

Olivines from tephra of the 1951 eruption of Fogo Volcano in Cabo Verde (DeVitre *et al.*, 2023), were also picked under binocular microscope and individually mounted in CrystalBond™. FI were revealed by grinding using 600–2000 grit wet paper and polish refined using 1 and 0.3 μm wet paper and alumina paste. These crystals were doubly polished for micro thermometric analyses. We analysed 63 FI in 12 crystals of this eruption *via* Raman and microthermometry.

1.2 Raman Spectroscopy FI CO₂

We collected Raman spectra using a WiTec Alpha 300R Raman spectrometer at the Department of Earth and Planetary Sciences at the University of California, Berkeley. We use a green solid state 532.046 nm laser focused as an excitation source with a 50x objective (x0.55NA, 9.1 mm focal distance) and 100x objective (x0.95NA, 4 mm WD). The system is equipped with TruePower system which allows for in-fiber power adjustments of <0.1 mW. We used a power of 6–12 mW. We used an FDCA built following the method of DeVitre *et al.* (2021) with an extended upper pressure limit from 35 to up to 68 MPa (through use of a sapphire window instead of fused silica-quartz) to produce calibration equations relating CO₂ density and Δ_{CO_2} for our instrument. These equations are available in DiadFit (Wieser and DeVitre, 2023) and have the same functional form as those reported in DeVitre *et al.* (2021) with updated coefficients.

Spectra for FI were collected at 37 °C, with temperature regulated at 37 °C using a Peltier thermoelectric stage with a centre hole fixed on a magnetic aluminum holder. Spectra were acquired with five accumulations of 45 s of integration time (total analytical time = 225 s) in a single window using 1800 grooves/mm ($\sim 0.54 \text{ cm}^{-1}$ spectral resolution) and a spectral centre of 1325 cm^{-1} . We discarded spectra with less than three points above the background (these yield spurious fits with up to >100 % error on fitting), those with high backgrounds interfering with the fit and those with normalised Intensity/FWHM < 200 according to the criteria of Yuan and Mayanovic (2017) as these cannot be fit confidently. A filtered total of 124 FI yielded results with 1σ in CO₂ density better than $\sim 0.02 \text{ g/mL}$ (Table S-1).

Neon (Ne) spectra were collected every ~ 10 –15 minutes using the same grating and spectral centre as the unknown and three accumulations of 45 s integration time, to correct for non-linearity of the Raman shift axis (Lin *et al.*, 2007; Wang *et al.*, 2011; Lamadrid *et al.*, 2017; DeVitre *et al.*, 2021).

All spectra were processed using the Python tool DiadFit v0.0.62 (Wieser and DeVitre, 2023). Spectra are baseline-subtracted prior to fitting (2nd degree polynomial baseline subtraction anchored on either side of peak of interest), and we fit a Pseudo-Voigt peak (mixed Gaussian and Lorentzian model) on each main CO₂ peak (1285 cm^{-1} and 1389 cm^{-1}). Voigt and Pseudo-Voigt functional forms are typically considered the most appropriate for symmetric Raman peaks (*e.g.*, single-phase CO₂ peaks and Neon emission lines; Yuan and Mayanovic, 2017). For fitting, CO₂ spectra were separated into three groups based on overall intensity of the spectra, and overlap between main peaks, hot bands (1270 cm^{-1} and 1410 cm^{-1}) and ¹³C (1370 cm^{-1}) such that additional peaks were simultaneously fit when needed to reduce the effect of residuals on the fit (Jupyter notebooks are included in the supplement). We corrected our data following the methods of Lamadrid *et al.* (2017) and DeVitre *et al.* (2021) using two known Ne emission lines (1117.086987 cm^{-1} and 1447.564622 cm^{-1}) that encompass the Fermi diad. A single Voigt peak is fit at 1446–1453 cm^{-1} for the upper line while two Voigt peaks (1113–1120 cm^{-1} and 1115–1122 cm^{-1}) are used for the lower line since it appears as a double-peak at our spectral resolution. We calculated the instrumental drift correction factor Ne_{coeff} as:

$$\text{Ne}_{\text{coeff}} = \left(\frac{\Delta \text{Ne}_{\text{known}}}{\Delta \text{Ne}_{\text{observed}}} \right) \quad (\text{S-1})$$



where ΔNe_{known} is the theoretical separation of the Ne emission lines in air and $\Delta Ne_{\text{observed}}$ is the measured separation of the same Ne emission lines on the Raman spectrum.

We then modelled the instrumental drift during each session as a polynomial function (typically 1st to 3rd degree polynomial, unless large temperature fluctuations happened during the session) relating Ne_{coeff} to time in seconds. Exact timestamps are extracted for each CO₂ spectrum and the appropriate Ne_{coeff} from the model is applied to correct the separation of the Fermi Diad. We also fit and calculated areas for SO₂ and CO₃ when observed on the spectra; these were fit as gaussian functions.

We calculated densities using the appropriate calibrated density equations for our instrument using DiadFit (Wieser and DeVitre, 2023). We estimated entrapment temperatures from the Fo content of the olivine (see below). We then calculated pressures from measured densities and estimated entrapment temperatures using the EOS of Span and Wagner (1996) and propagated uncertainty using Monte Carlo simulations. Finally, we calculated the depths of entrapment using the crustal density model of Ryan (1987), described in Lerner *et al.* (2021) for Hawai‘i.

1.3 Quantifying Uncertainty and Reproducibility of Measurements of Fluid Inclusions

Uncertainties on fluid inclusion pressures were propagated in DiadFit, using Monte Carlo simulations considering 50 K uncertainty on the Temperature (see section 1.5) and 1 σ uncertainty on density from peak-fit uncertainties on CO₂ spectra and the uncertainty in the Ne correction model estimated by DiadFit. The majority of data presented in the paper was fitted with DiadFit version v0.0.62. This version propagates the uncertainty in peak position into calculated densities. A newer version of DiadFit (v0.0.78) that was released recently also accounts for the error from the densimeter and drift correction model. To assess differences between these errors, we refit a subset of Raman data (17 October 2022; see Table S-3 and data repository) that encompasses most CO₂ densities found in our study (Wieser and DeVitre, 2023). We did not apply filters for bad spectra (*e.g.*, high background, too little intensity/number of points to fit) for this exercise. It is immediately apparent that the error for our measurements predominantly arises from the error involved in fitting Diad peaks (Fig. S-1), and that the error on the densimeter and Ne line correction plays only a minor role in most cases (Fig. S-1c, d; <10%). Additionally, the densities and associated errors calculated by version v0.0.62 are not significantly different from those calculated by v0.0.78 (Fig. S-2), and both lie on a 1:1 line. The densities calculated with v.0.078 are within 0.004 g/cm³ of those calculated with v.0.062 and except for four data points, the majority are within 0.001 g/cm³. The calculated errors are for the most part within 0.002 g/cm³ except for two points (one at 0.004 g/cm³ and one at 0.01 g/cm³). We note that these two datapoints as well as some others were discarded in the final dataset due to low intensity and/or high backgrounds which largely accounts for the high fitting error. Overall, this shows that for the samples examined in this study, the peak fitting errors from v0.0.62 are a reasonable estimate, and complete refitting of the dataset is not justified.



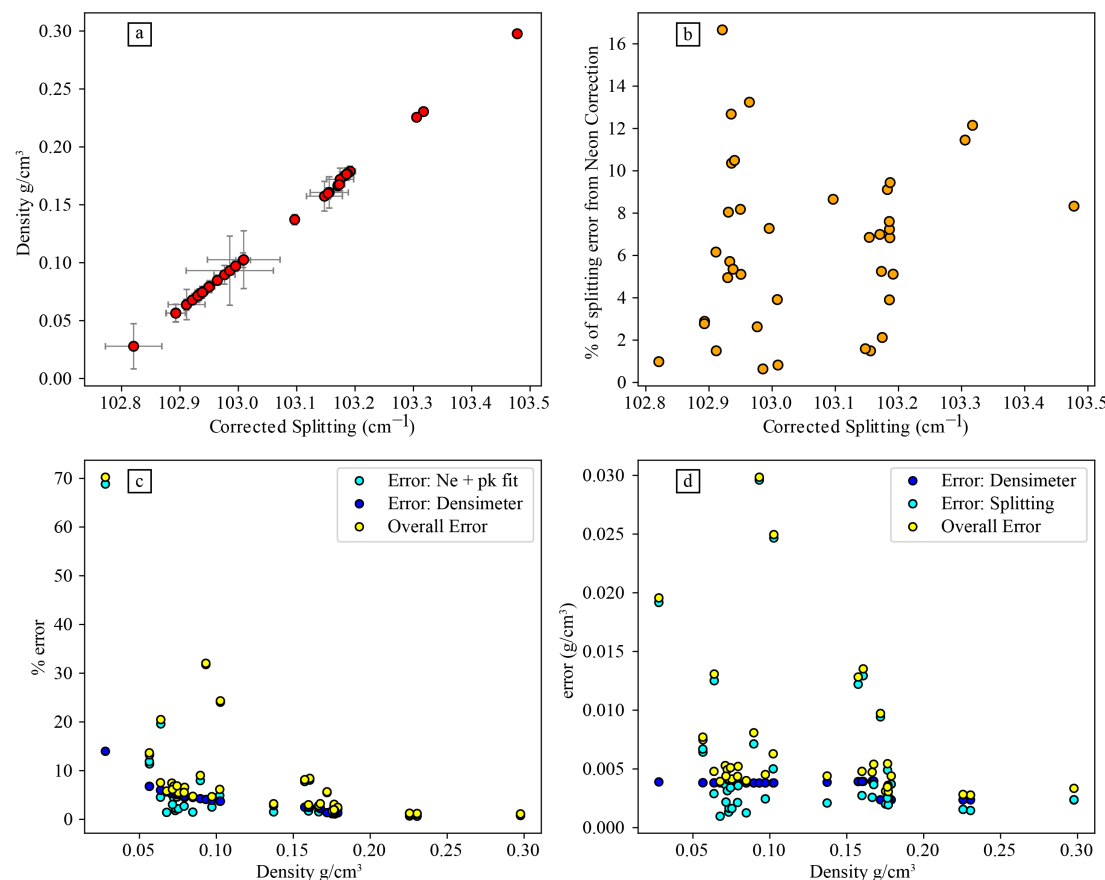


Figure S-1 Refit Raman data from 17 October 2022 using DiadFit v0.0.78. **(a)** Separation of the Fermi Diad vs. CO_2 density with error bars shown in black. **(b)** Percentage of the error on the Fermi Diad separation that is due to the Neon Correction. **(c)** Percentage of error in CO_2 density vs. CO_2 density. Yellow dots are the overall error (from all sources), cyan dots are the error from peak fitting and neon correction alone and blue dots are the error from the densimeter only. **(d)** Absolute error in CO_2 density vs. CO_2 density. Yellow dots are the overall error (from all sources), cyan dots are the error from peak fitting and neon correction alone and blue dots are the error from the densimeter only.

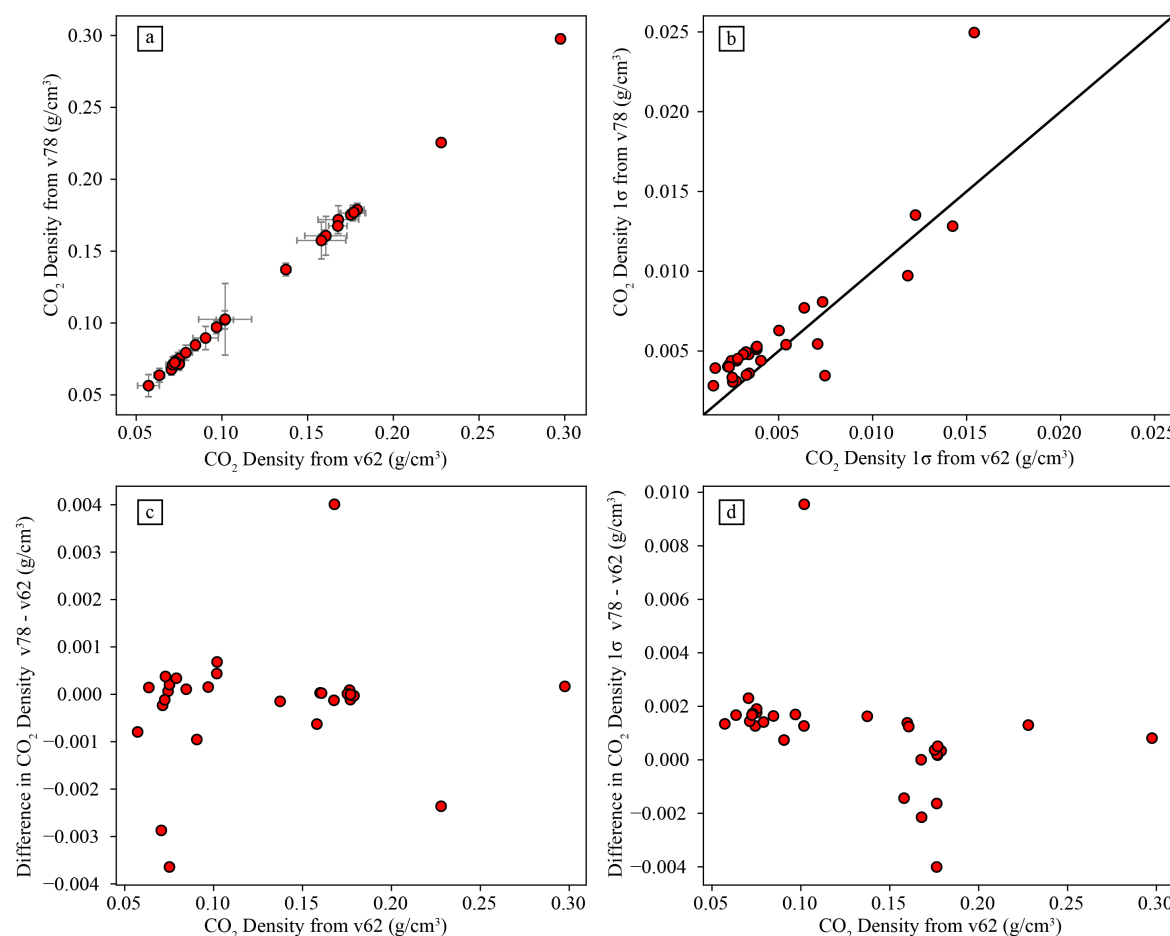


Figure S-2 Refit Raman data from 17 October 2022 using DiadFit v0.0.78 vs. original data fit using DiadFit v0.0.62. **(a)** CO₂ density from version v0.0.78 vs. from version v0.0.62 with error bars shown in black. **(b)** CO₂ density 1σ error from version v0.0.78 vs. from version v0.0.62. **(c)** Difference in CO₂ density from v78 and CO₂ density from v62. **(d)** Difference in CO₂ density 1σ error from v78 and CO₂ density 1σ from v62.

We also assessed the reproducibility of our measurements based on repeated analyses of single fluid inclusions (Fig. S-3). For repeated measurements, the standard deviation is no higher than 0.02 g/cm³, even when the measurements were repeated on different days (Fig. S-3a, b). Further, the 1σ error output from DiadFit is similar to the standard deviation of repeated measurements and is often slightly higher. Overall, only one measurement in our reported dataset has a 1σ > 0.02 g/cm³, which indicates that the use of a CO₂ density error of ~0.02 g/cm³ in the Monte Carlo error simulations is appropriate to describe the error in our dataset. This also matches the findings of Dayton *et al.* (2023) based on their repeated measurements using identical instrument and calibration hardware.

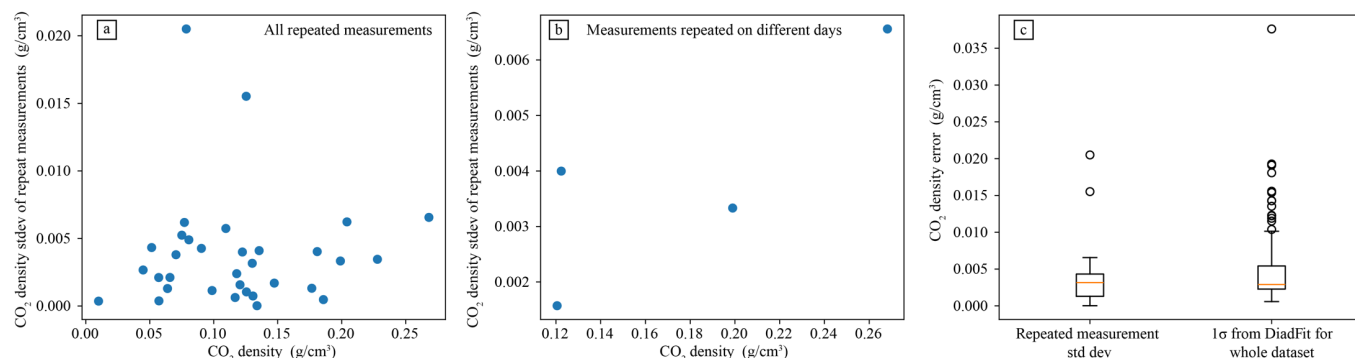


Figure S-3 Comparison of error from DiadFit and reproducibility of repeated measurements. (a) Standard deviation of repeated measurements *vs.* CO₂ density. This plot includes measurements that were repeated on the same day (consecutive repeated measurements) as well as those that were repeated on a different day. (b) Standard deviation of repeated measurements *vs.* CO₂ density considering only measurements with repeats on different days (for the same fluid inclusion at least one of the repeats was on a different day). (c) Box plots of CO₂ density error for two groups: repeated measurements (this is the standard deviation of N repeated measurements) and the reported error calculated from DiadFit. This demonstrates the error estimated by DiadFit is a good match to the error determined by repeated measurements.

1.4 Microthermometry of FI

For samples with bulk CO₂ densities above the critical density of CO₂ (~0.45 g/mL), we conducted microthermometry experiments to obtain the freezing and homogenisation temperatures and calculate an independent estimate of the CO₂ density of the FI. It was not possible to obtain microthermometric data for FI that homogenise to vapor, as it is difficult to observe the homogenisation of the thin liquid film into vapor in our samples. These experiments were conducted using a Linkam THMSG600 heating and freezing stage, with environmental control from -195 °C to +600 °C, equipped with a liquid nitrogen cooling pump allowing for cooling rates from 0.01 to 150 °C/min. We used a CO₂-H₂O standard to calibrate the melting temperature of CO₂ (-56.6 °C) and a pure H₂O standard to calibrate the melting temperature (0.0 °C). All experiments were done using the cycling technique (Hansteen and Klügel, 2008) to ensure that homogenisation was completed. We then converted the homogenisation temperatures to CO₂ density using the EOS of Span and Wagner (1996) implemented in DiadFit (Wieser and DeVitre, 2023). All FI were found to have melting temperatures of -56.5 ± 0.1 °C (Fig. S-4a), indicating that they are pure CO₂.

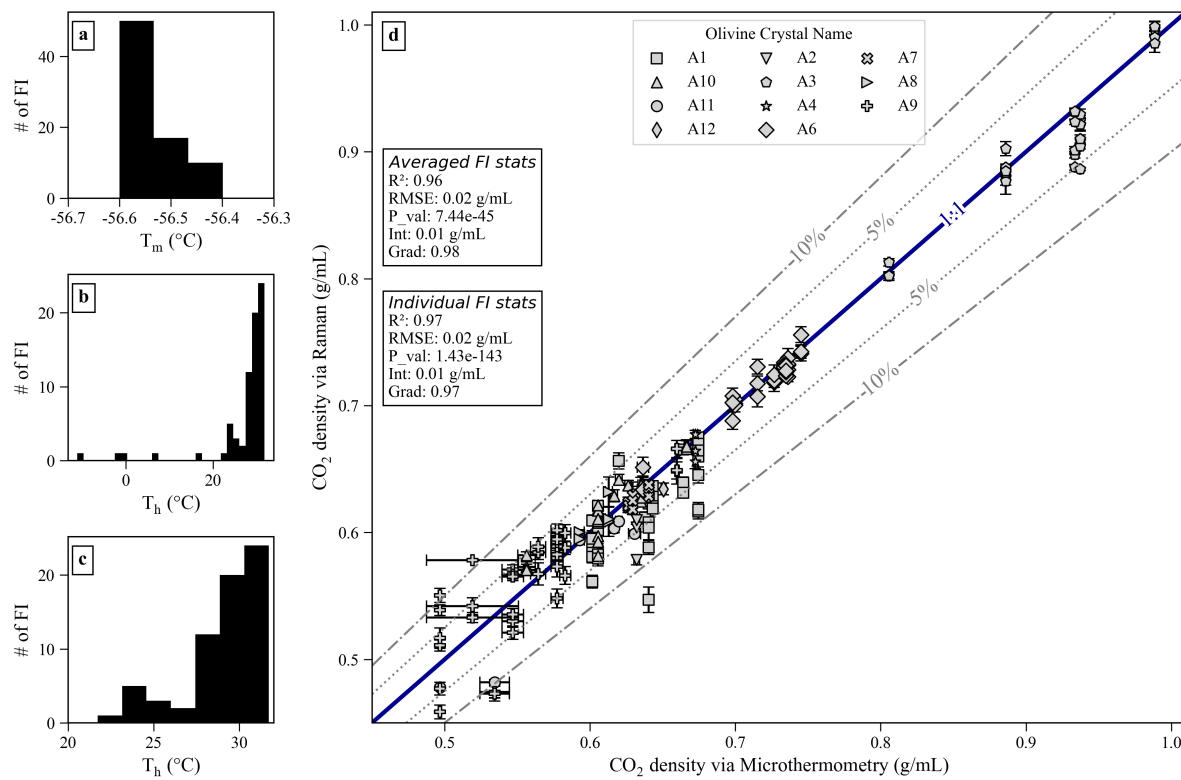


Figure S-4 CO₂ densities *via* microthermometry *versus* calibrated Raman Spectroscopy. **(a)** Freezing temperatures of FI. **(b)** Homogenisation temperatures of FI (all FI homogenised to liquid). **(c)** Close-up of panel (b). **(d)** Density *via* Raman *versus* density *via* micro thermometry. FIs in the same crystal are plotted with the same symbol. Error bars for Raman-based CO₂ densities are propagated fitting + Neon correction uncertainties while error bars for microthermometry are the standard deviation of homogenisation temperatures obtained during cycling.

Under Raman spectroscopy, none of the FI analysed had detectable amounts of any other gases, however they contained variable amounts of carbonate. Homogenisation temperatures ranged from -11.1 ± 0.2 °C to $+31.6 \pm 1$ °C (Fig S-1b, c), measurements with homogenisation temperatures close to critical were more difficult to perform and the uncertainty on the temperature is therefore higher, limited by the high $\Delta\rho/\Delta T$ and the accuracy of the temperature controller of the stage. We only calculate and report CO₂ densities from microthermometry when the homogenisation temperature was determined with reasonable confidence. Peak-fitting and drift and precision account for most of the uncertainty for Raman (see Fig. 8 in Wieser and DeVitre, 2023), while the uncertainty for microthermometry can be attributed to difficulty in observing the phase homogenisation near and/or below the critical density of CO₂, thermocouple accuracy and precision of thermal control. For densities close to critical (~ 0.45 g/mL), the uncertainty on microthermometry measurements significantly increases due to much higher $\Delta\rho/\Delta T$ —such that very small uncertainties in the homogenisation temperature can cause much larger uncertainties in the density (Hansteen and Klügel, 2008).

1.5 Host Olivine Chemistry

Spot analyses of host olivines were conducted using a JEOL JXA-8230 EPMA in the Mineral and Microchemical Analysis Facility at Stanford University. Counting statistics and other analytical conditions



along with repeated analyses of secondary standards (San Carlos Olivine, Stillwater olivine; Jarosewich *et al.*, 1980) are presented in Table S-5. We note that melt inclusion olivine hosts reported in Wieser *et al.* (2021) were analysed using the University of Cambridge's Cameca SX100 EPMA in the Department of Earth Sciences. For consistency in our comparisons, we correct the Fo contents (mol %) of our fluid inclusion olivine hosts obtained from the Stanford EPMA data to Fo contents that would have been obtained had they been analysed on the Cambridge EPMA instead. To do this, we analysed spots on a subset of olivines from Wieser *et al.* (2021) which had previously been analysed at Cambridge, based on detailed BSE maps. We then performed a linear regression of olivine host Fo contents from Stanford and Cambridge and use the equation to correct our fluid inclusion olivine host Fo content data. The equation is as follows: $Fo_{\text{Cambridge}} = 0.9815 \times Fo_{\text{Stanford}} + 0.893$.

Entrapment temperatures were estimated from the host olivine Fo content by developing an olivine-only thermometer suitable for Kīlauea. The Fo content of an olivine is a function of the MgO and FeO_T content of the liquid from which it equilibrates with, the Ol-Liq partition coefficient, and the proportion of Fe³⁺ in the liquid. Fortunately, Ol-saturated liquids at Kīlauea have a relatively constant FeO content (see Fig. S-5). Thus, if the Fo content is known, the K_D is known, the Fe³⁺ ratio is known, and the FeO_T content can be relatively constant, the Fo content can be related to MgO, which in turn, can be related to temperature at Kīlauea.

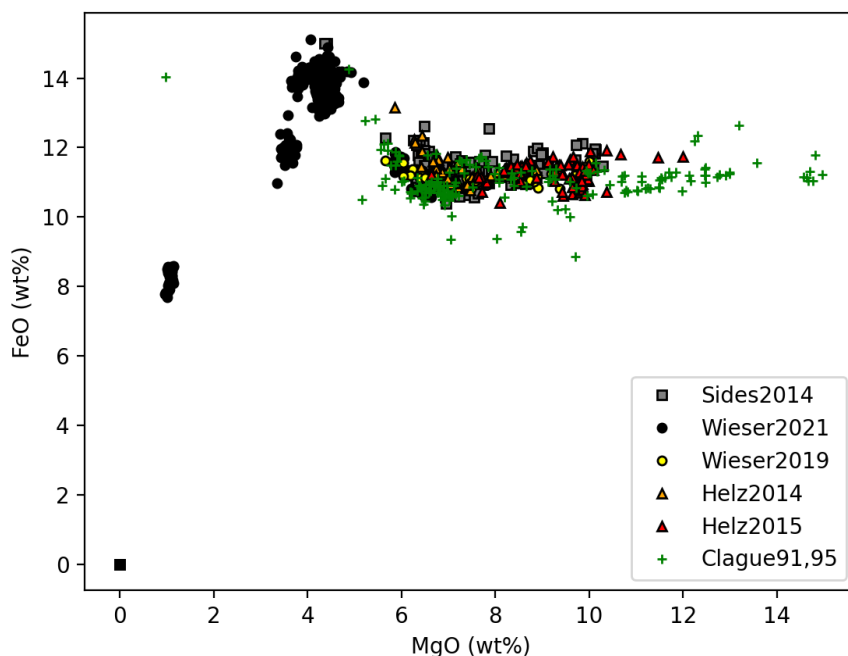


Figure S-5 Compiled glass data used to calibrate an Ol-only thermometer (Clague and Bohrson, 1991; Clague *et al.*, 1995; Helz *et al.*, 2014, 2015; Sides *et al.*, 2014a, 2014b; Wieser *et al.*, 2019, 2021).

To calibrate the Ol-only thermometer, we calculated a liquid-only temperature using the new MgO-thermometer of Shea *et al.* (2022) for each liquid in our compiled dataset. We also calculated an equilibrium olivine content using the K_D model of Shea *et al.* (2022), assuming $\text{Fe}^{3+}/\text{Fe}_T = 0.15$ (Moussallam *et al.*, 2016; Helz *et al.*, 2017; Lerner *et al.*, 2021). We then fit a 3rd degree polynomial between temperature and Ol Fo content (Fig. S-6). We also show the polynomial that would result from using $\text{Fe}^{3+}/\text{Fe}_T = 0.2$ instead. This is well within the ± 50 K uncertainty used for temperature for the Monte-Carlo simulations (red dashed lines).

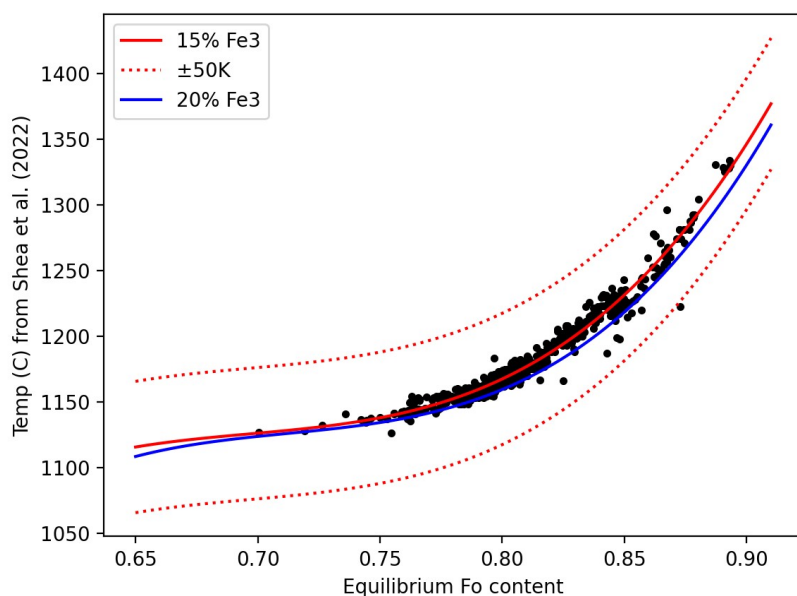


Figure S-6 3rd degree polynomial fit between equilibrium Fo content and temperature calculated from the glass composition using the thermometer of Shea *et al.* (2022).

We tested the success of this Ol-only thermometer on the experimental data used to calibrate the expressions of Shea *et al.* (2022). We note that these experimental liquids have far more diversity in FeO content than natural Kīlauea liquids, which explains the larger discrepancies that exist. If we restrict comparison to liquids within the mean $\pm 1\sigma$ of the observed distribution of Kīlauean liquids, we can see the method is successful within the ± 50 K uncertainty allocated for Monte Carlo methods (pink box, Fig. S-7).

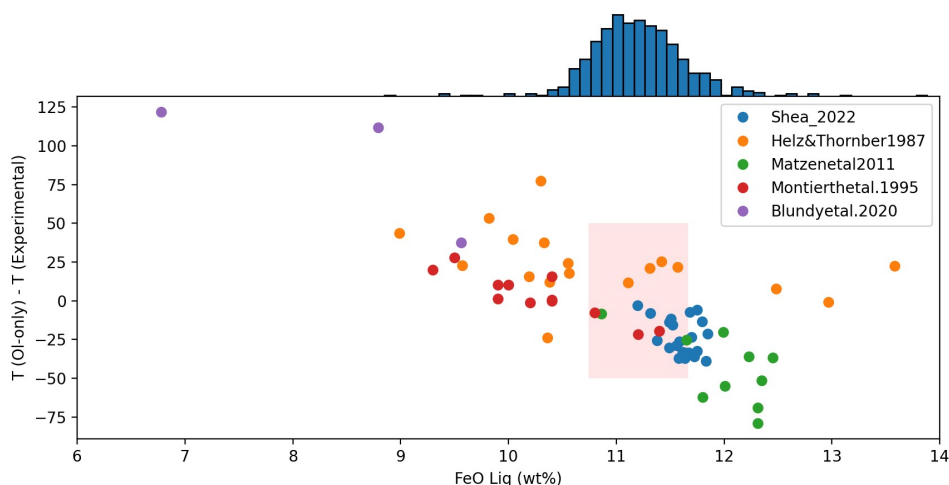


Figure S-7 Assessing the Ol-only thermometer on the calibration dataset of Shea *et al.* (2022). The distribution of FeO contents in natural Kīlauea liquids is shown with the blue histogram. In the pink shaded box, we highlight experimental liquids within the mean $\pm 1\sigma$ of this distribution. These experiments lie well within the $1\sigma = 50$ K uncertainty allocated for entrapment temperatures. Data from Helz and Thornber (1987), Montierth *et al.* (1995), Matzen *et al.* (2011), Blundy *et al.* (2020), Shea *et al.* (2022).

1.6. Estimating SO₂/CO₂ Ratios in FI

To estimate the SO₂ fraction in our FI, we calculated the area under the SO₂ peak ($\sim 1151 \text{ cm}^{-1}$). We first background subtracted using the same method as for CO₂ and Neon spectra and then fit a spline to the SO₂ spectrum.

2. Statistical Significance of the MI vs. FI Recorded Pressures

To assess whether the pressures recorded by MI and FI are statistically different, we conducted Kolmogorov–Smirnov (KS) tests. Given the relatively small sample set sizes ($n < 50$), we performed both sample KS tests and Monte-Carlo KS tests using a Python3 routine in which we resampled 1000 times considering the uncertainties of each independent measurement. We compare the MI distributions for MI saturation pressures calculated using five different volatile solubility models (MagmaSat, Ghiorso and Gualda, 2015; MafICH, Allison *et al.*, 2022; VolatileCalc, Newman and Lowenstern, 2002; and those of Iacono-Marziano *et al.*, 2012 and Shishkina *et al.*, 2014) with the pressure distribution from our new FI data (Fig. S-8). We note that there are very large variations in the MI saturation pressures when using different solubility models, which by themselves can largely account for the difference in the distributions (Fig. S-9). If one considers the MagmaSat solubility model, while the sample KS statistics appear significant (which would suggest that the FI are underestimating the magma storage pressures), when we consider the uncertainty on both the FI and particularly the MI measurements, the Monte-Carlo KS statistic is no longer significant for any of the three events. This suggests that the FI are predicting the same entrapment pressures as the MI, within the uncertainty of the measurements.



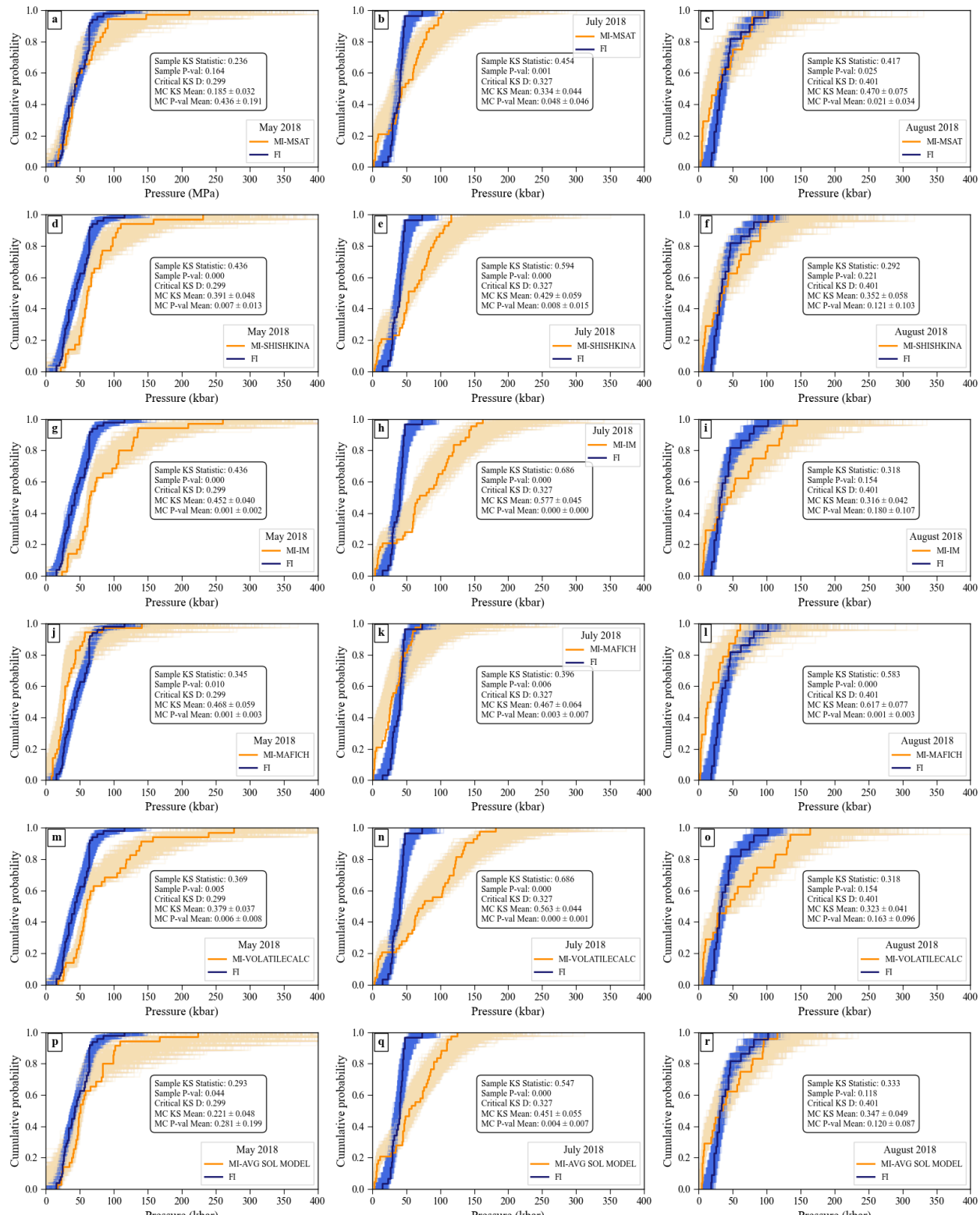


Figure S-8 Monte Carlo KS tests on cumulative distributions of pressures for FI (blue) and MI (orange) using different solubility models for each eruptive event: (a–c) MagmaSat ('MSAT', Ghiorio and Gualda, 2015); (d–f) Shishkina *et al.* (2014, 'SHISHKINA'); (g–i) Iacono-Marziano *et al.* (2012; 'IM'); (j–l) MafiCH (Allison *et al.*, 2022); (m–o) VolatileCalc (Newman and Lowenstern, 2002); (p–r) Average Solubility model (standard deviation as uncertainty).



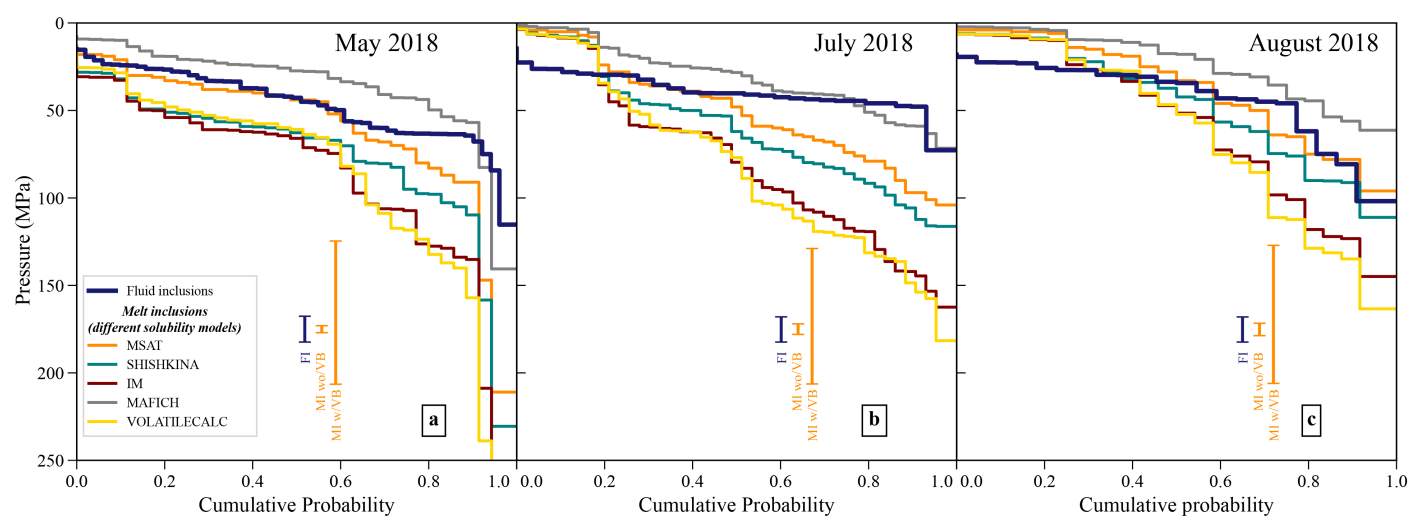


Figure S-9 Pressure CDF for comparing fluid and melt inclusion pressures for (a) May 2018, (b) July 2018 and (c) August 2018 using five different solubility models: MagmaSat ('MSAT'; Ghiorso and Gualda, 2015), Shishkina *et al.* (2014; 'SHISHKINA'), Iacono-Marziano *et al.* (2012; 'IM'), MafICH (Allison *et al.*, 2022), and VolatileCalc (Newman and Lowenstern, 2002).

3. Effect of H₂O mol % in Fluid on Calculated Densities and Pressures

In relatively shallow systems like Kīlauea, the exsolved vapour phase will not be pure CO₂, but will contain some fraction of H₂O. When performing fluid inclusion studies on mixed fluids, it is generally assumed that the H₂O has been lost from the fluid inclusion. Then, the measured CO₂ density is corrected based on the molar fraction of H₂O and molar ratios (see Hansteen and Klügel, 2008). This bulk density is then entered into a mixed H₂O–CO₂ equation of state to calculate pressure.

To estimate the mol fraction of H₂O in the exsolved fluid, we examined melt inclusion data from Wieser *et al.* (2021). The solubility model MagmaSat returns the calculated pressure, and $X_{\text{H}_2\text{O}}$ at the point of vapour saturation. For the 2018 eruption, it is difficult to estimate the initial H₂O content at the time of melt and fluid inclusion entrapment, because H₂O was reset through diffusive re-equilibration with the carrier melt transporting crystals down the East Rift Zone. However, it has been suggested that the reservoir melts were likely drier than normal Kīlauea magmas due to mixing and degassing of summit lake lavas over the decade prior (Lerner *et al.*, 2021). To encompass this uncertainty, we show $X_{\text{H}_2\text{O}}$ calculated using the measured H₂O content, and 0.5 wt. % H₂O, which encompasses the higher end of the range at Kīlauea over the last few hundred years (Fig. S-10, red and blue dots, respectively). We also calculated the mean of the two (Fig. S-10b, green dots).



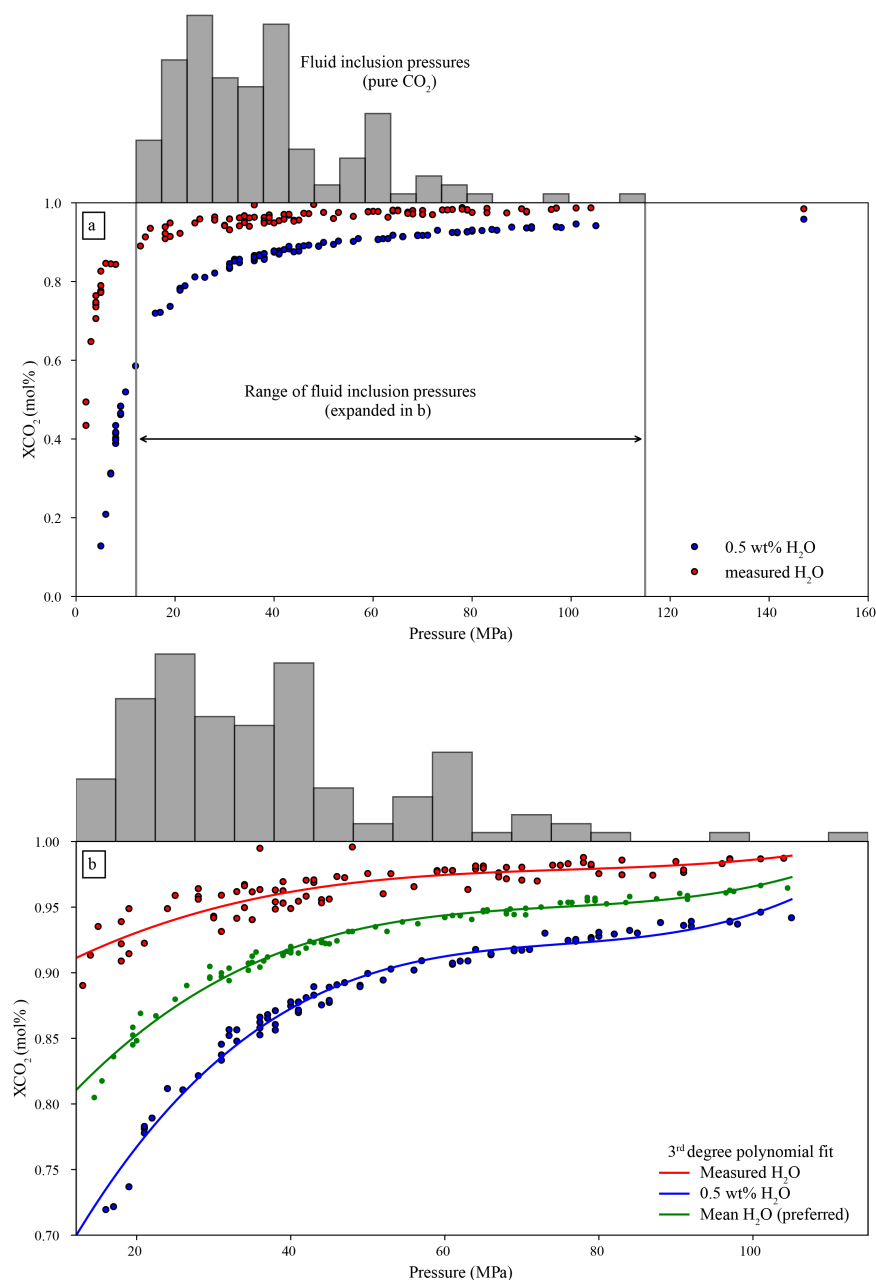


Figure S-10 $X\text{CO}_2$ values from Wieser *et al.* (2021). **(a)** The entire range of measured pressures. **(b)** Enlarged view of only the pressure range observed in fluid inclusions along with 3rd degree polynomial fits. Based on inferences of H_2O drainback and degassing (Lerner *et al.*, 2021), we use $X\text{CO}_2$ shown by the green polynomial, although we consider the uncertainty introduced by $X\text{CO}_2$ between the red and blue polynomials (measured H_2O contents, red dots, lower plausible limit), and upper limit Kīlauea H_2O contents (blue dots, 0.5 wt. %, upper plausible limit).

To perform the correction, we regressed pressure *vs.* $X\text{CO}_2$ (equivalent to $1 - X\text{H}_2\text{O}$) using a 3rd degree polynomial (Fig. S-10b) for measured H_2O contents, 0.5 wt. % H_2O and the mean H_2O values. This means for each fluid inclusion we can allocate an approximate $X\text{H}_2\text{O}$ value as $X\text{H}_2\text{O} = 1 - X\text{CO}_2$. We then calculated pressure using the mixed CO_2 – H_2O EOS of Duan and Zhang (2006) implemented in DiadFit v0.0.80. Given



that our initial pressures were calculated using a pure CO₂ EOS, we iterated four times to converge towards a final corrected pressure. We note that the corrected pressures and associated uncertainties are within the pure CO₂ pressures and the uncertainty estimated by the Monte Carlo simulations (Fig. S11). We used the $X\text{CO}_2$ value from the green (middle) scenario, but consider the uncertainty introduced by $X\text{CO}_2$ values between the blue and red lines.

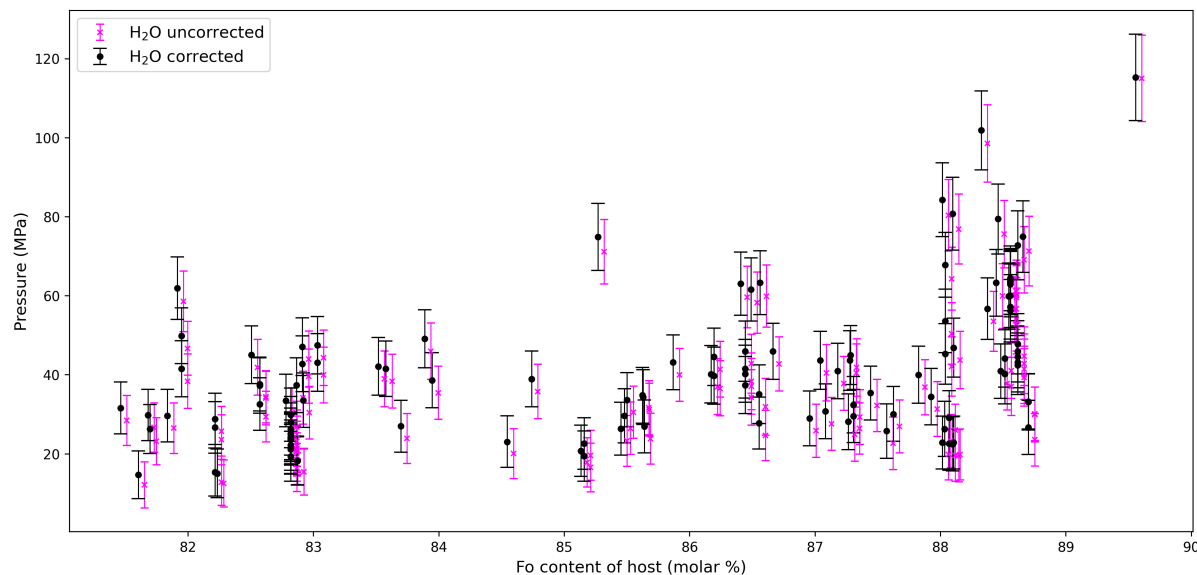


Figure S-11 Fluid inclusion pressures as a function of the Fo content of the olivine hosts. Black markers are H₂O corrected pressures, with corresponding uncertainties considering the minimum and maximum water content ranges from Figure S10 as well as the uncertainty from the Monte Carlo simulations for the pure CO₂ EOS pressures, summed in quadrature. Magenta markers show the pure CO₂ EOS pressures and are artificially offset in Fo content by 0.05 to aid visibility.

4. Fluid % Effect on Calculated Densities and Pressures

Magmatic fluid inclusions are often trapped with variable small amounts of silicate melt. We estimated the proportion of exsolved fluid to silicate melt using FIJI (Schindelin *et al.*, 2012). We filtered out of the dataset any inclusion <80 % exsolved fluid. In Figures S-12 and S-13, we plot the measured CO₂ density of FI in the same crystals, which have variable amounts of exsolved fluid. We also individually plot the FI in each crystal in subsequent panels. We found no clear trends indicating that FI with small amounts of silicate melt (<20 %) are likely to record the same conditions as those with nearly no melt at all. Some crystals show a weak relationship where FI with no melt or very little melt have record the highest densities. However, we recognise the dataset is much too small to conclude on this matter. Future work is required to constrain whether any significant relationship exists. For this study, we consider that FI with >80 % exsolved fluid offer a suitable record of pressure. This is consistent with previous work indicating that exchange of CO₂ with the melt is negligible in inclusions that trap predominantly the vapor phase (little melt) (Steele-MacInnis *et al.*, 2017).

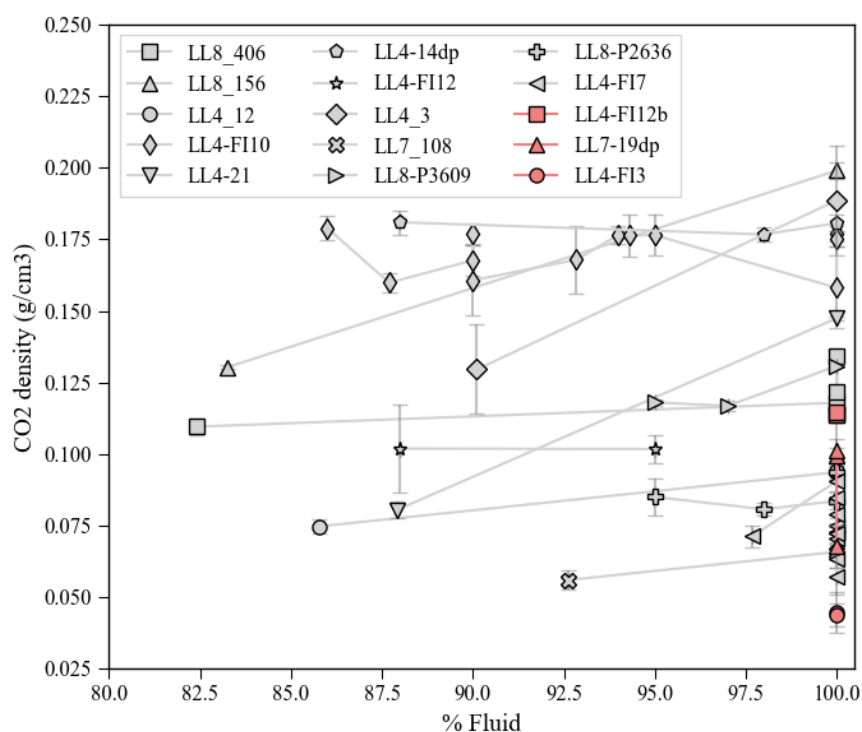
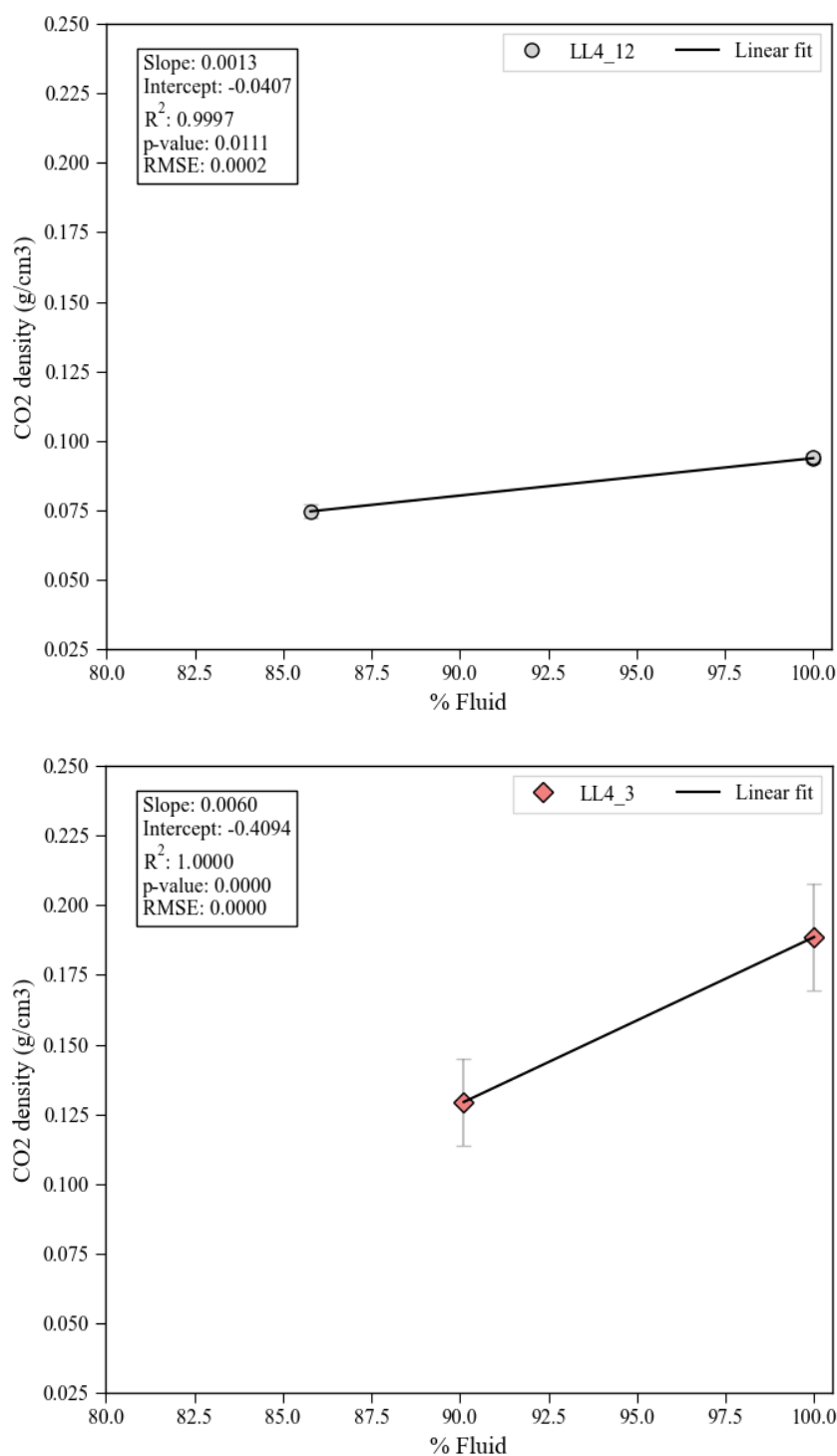
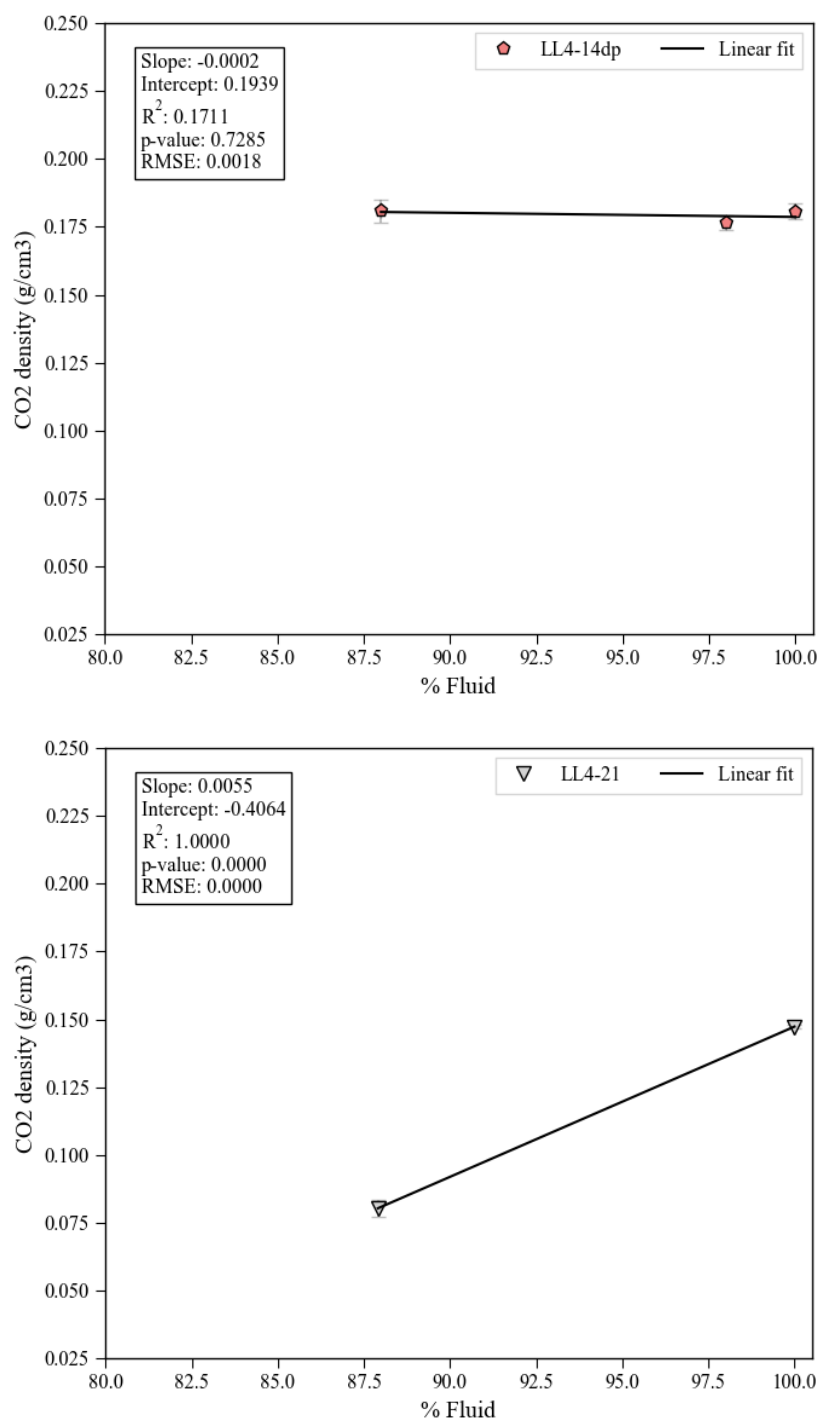
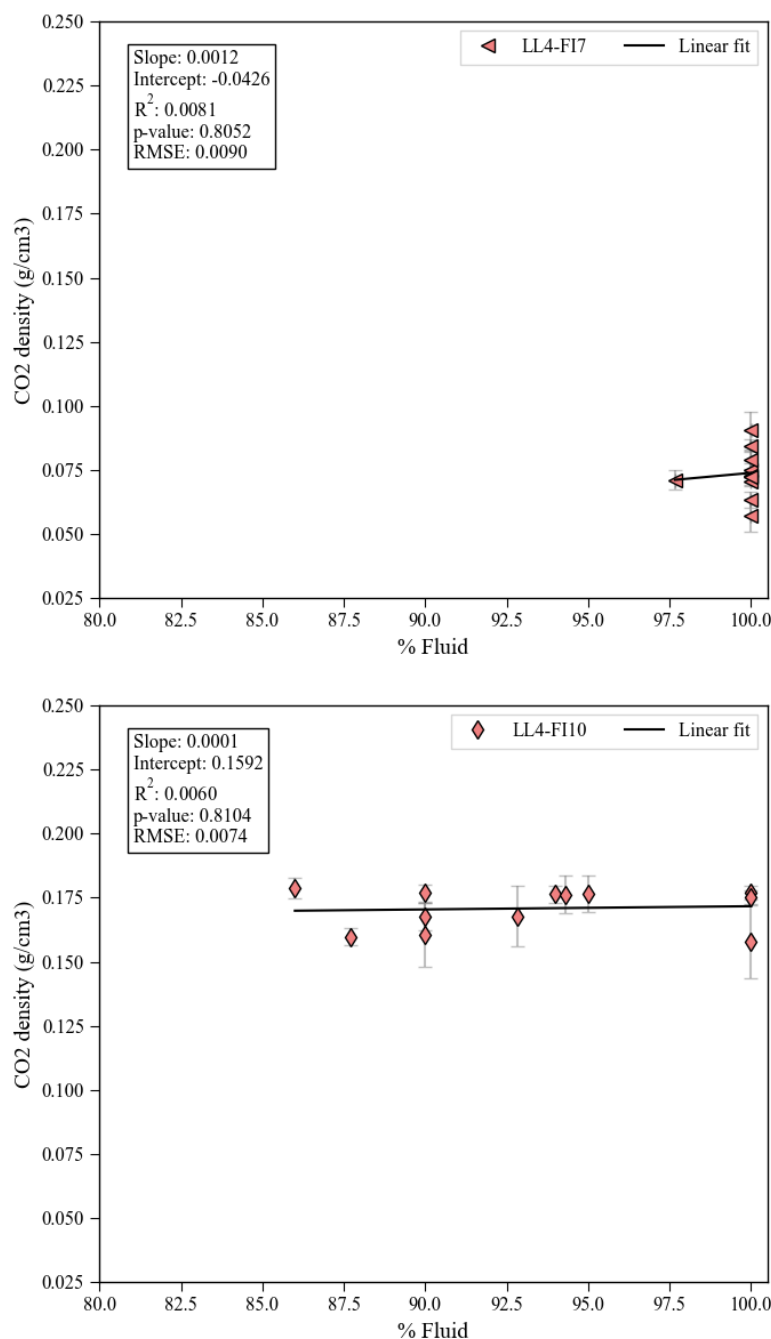


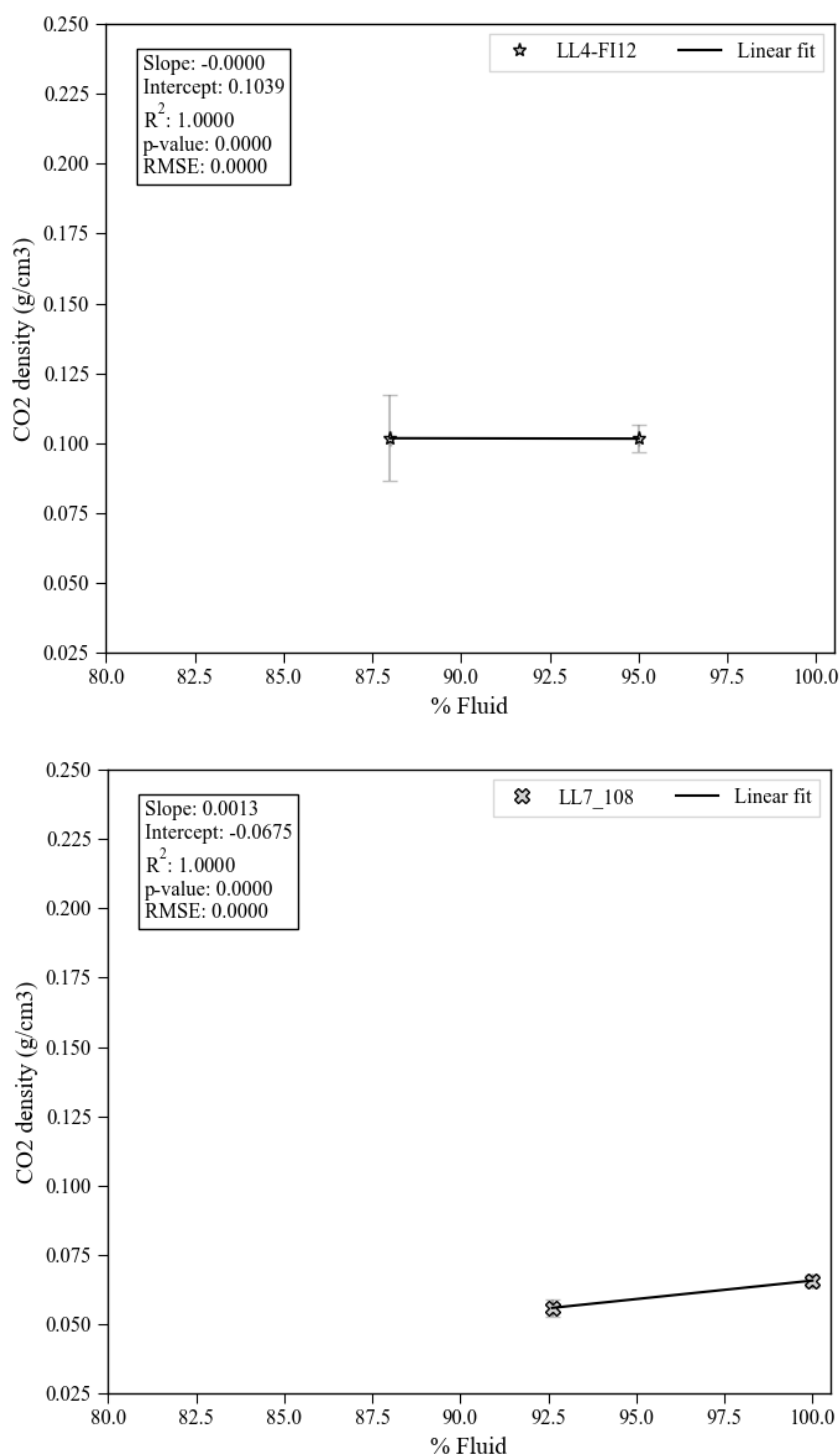
Figure S-12 Measured CO₂ density of FI against the % exsolved fluid for FI “pairs”, *i.e.* FI found in the same crystals and within relative proximity to each other with apparently similar genetic relationships.

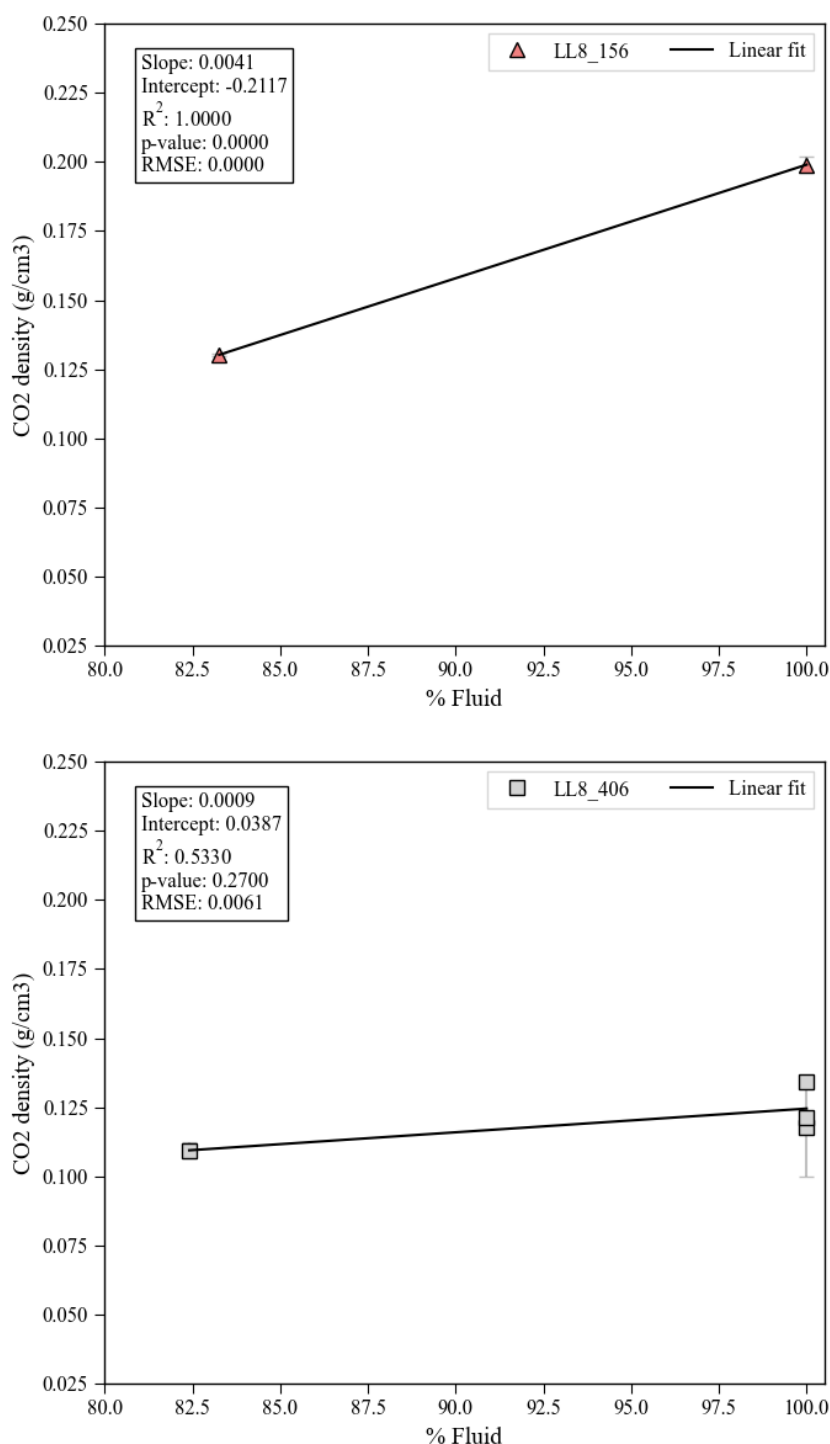
Figure S-13 Single crystal plots (pages SI-16 to SI-21). Measured CO₂ density of FI against the % exsolved fluid for FI “pairs”, *i.e.* FI found in the same crystals and within relative proximity to each other with apparently similar genetic relationships.

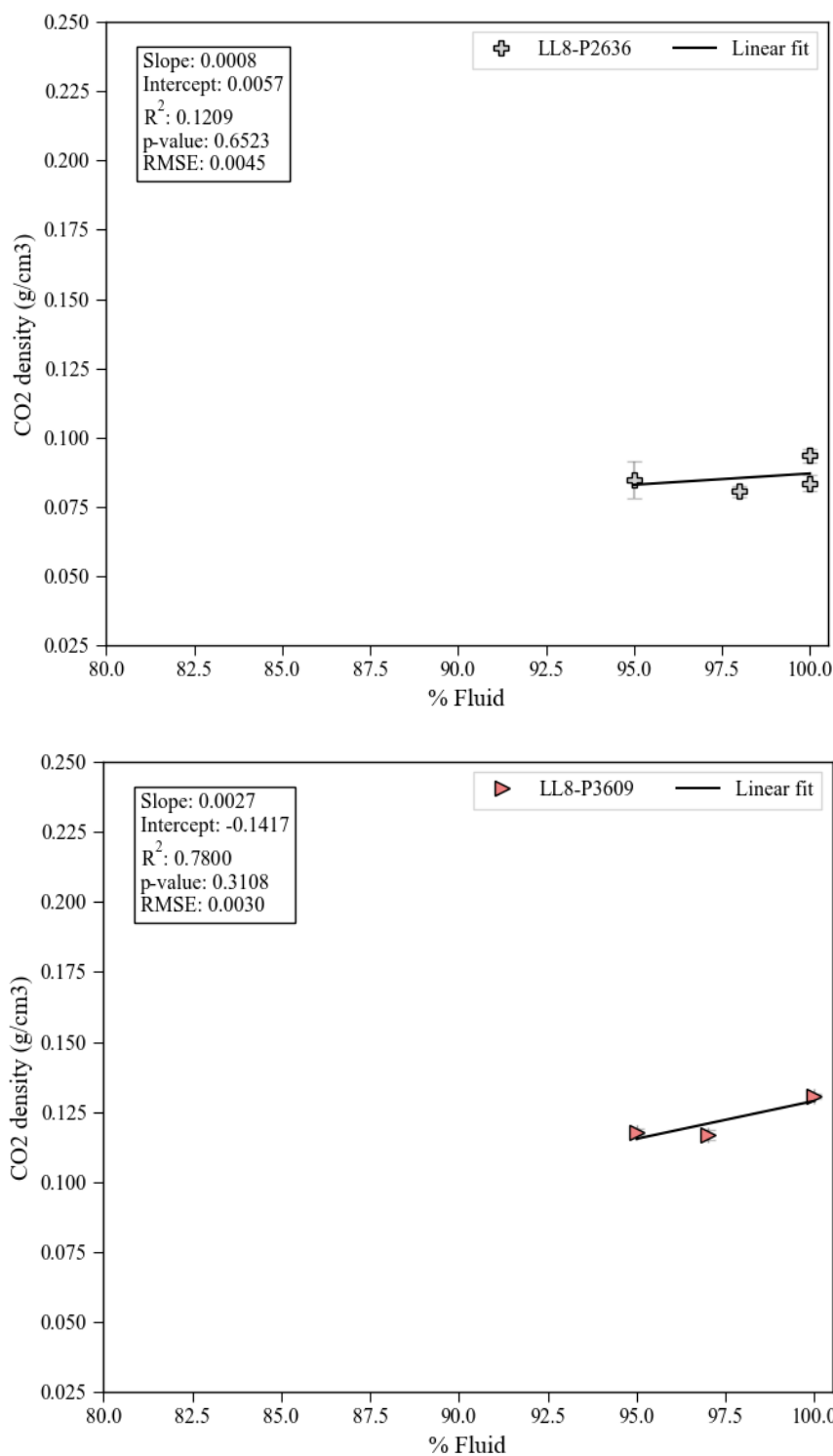












Supplementary Tables

Table S-1 Full data for each Kīlauea 2018 LERZ fluid inclusion (Raman, host olivine major element chemistry, pressure and depth calculations, and textural relationships. This is filtered for bad spectra and fluid % > 80). To see all analyses, unfiltered, unaveraged, or raw data, refer to the data repository.

Table S-2 CO₂ densities obtained *via* Raman and microthermometry for Fogo fluid inclusions. Note that in this table, repeated Raman measurements have already been averaged. For all analyses, refer to Table S-6.

Table S-3 Comparison of data fit by DiadFit v62 and DiadFit v78, for error assessment.

Table S-4 Comparison of error from peak-fitting and densimeter (output as 1sig from DiadFit) with uncertainty from repeated analyses.

Table S-5 Secondary olivine standards run for electron microprobe data; headers are the same as in Table S-1.

Table S-6 CO₂ densities obtained *via* Raman and microthermometry for all Fogo fluid inclusions. Note that in this table, repeated Raman measurements have NOT been averaged.

Table S-7 Supplementary dataset from Wieser *et al.* (2021).

Tables S-1 to S-7 are available for download (.xlsx) from the online version of this article at <https://doi.org/10.7185/geochemlet.2404>.

Supplementary Image Database

Supplementary images of fluid inclusions in their host crystals are available for download (.pdf) from the online version of this article at <https://doi.org/10.7185/geochemlet.2404>.

Supplementary Information References

Allison, C.M., Roggensack, K., Clarke, A.B. (2022) MafiCH: a general model for H₂O–CO₂ solubility in mafic magmas. *Contributions to Mineralogy and Petrology* 177, 40. <https://doi.org/10.1007/s00410-022-01903-y>

Blundy, J., Melekhova, E., Ziberna, L., Humphreys, M.C.S., Cerantola, V., Brooker, R.A., McCammon, C.A., Pichavant, M., Ulmer, P. (2020) Effect of redox on Fe–Mg–Mn exchange between olivine and melt and an oxybarometer for basalts. *Contributions to Mineralogy and Petrology* 175, 103. <https://doi.org/10.1007/s00410-020-01736-7>

Clague, D.A., Bohrson, W.A. (1991) Origin of xenoliths in the trachyte at Puu Waawaa, Hualalai Volcano, Hawaii. *Contributions to Mineralogy and Petrology* 108, 439–452. <https://doi.org/10.1007/BF00303448>

Clague, D.A., Moore, J.G., Dixon, J.E., Friesen, W.B. (1995) Petrology of Submarine Lavas from Kilauea's Puna Ridge, Hawaii. *Journal of Petrology* 36, 299–349. <https://doi.org/10.1093/petrology/36.2.299>



Dayton, K., Gazel, E., Wieser, P., Troll, V.R., Carracedo, J.C., La Madrid, H., Roman, D.C., Ward, J., Aulinas, M., Geiger, H., Deegan, F.M., Gisbert, G., Perez-Torrado, F.J. (2023) Deep magma storage during the 2021 La Palma eruption. *Science Advances* 9, eade7641. <https://doi.org/10.1126/sciadv.ade7641>

DeVitre, C.L., Allison, C.M., Gazel, E. (2021) A high-precision CO₂ densimeter for Raman spectroscopy using a Fluid Density Calibration Apparatus. *Chemical Geology* 584, 120522. <https://doi.org/10.1016/j.chemgeo.2021.120522>

DeVitre, C.L., Gazel, E., Ramalho, R.S., Venugopal, S., Steele-MacInnis, M., Hua, J., Allison, C.M., Moore, L.R., Carracedo, J.C., Monteleone, B. (2023) Oceanic intraplate explosive eruptions fed directly from the mantle. *Proceedings of the National Academy of Sciences* 120, e2302093120. <https://doi.org/10.1073/pnas.2302093120>

Duan, Z., Zhang, Z. (2006) Equation of state of the H₂O, CO₂, and H₂O–CO₂ systems up to 10 GPa and 2573.15 K: Molecular dynamics simulations with ab initio potential surface. *Geochimica et Cosmochimica Acta* 70, 2311–2324. <https://doi.org/10.1016/j.gca.2006.02.009>

Ghiorso, M.S., Gualda, G.A.R. (2015) An H₂O–CO₂ mixed fluid saturation model compatible with rhyolite-MELTS. *Contributions to Mineralogy and Petrology* 169, 53. <https://doi.org/10.1007/s00410-015-1141-8>

Hansteen, T.H., Klügel, A. (2008) Fluid Inclusion Thermobarometry as a Tracer for Magmatic Processes. *Reviews in Mineralogy and Geochemistry* 69, 143–177. <https://doi.org/10.2138/rmg.2008.69.5>

Helz, R.T., Thornber, C.R. (1987) Geothermometry of Kilauea Iki lava lake, Hawaii. *Bulletin of Volcanology* 49, 651–668. <https://doi.org/10.1007/BF01080357>

Helz, R.T., Clague, D.A., Sisson, T.W., Thornber, C.R. (2014) Petrologic insights into basaltic volcanism at historically active Hawaiian volcanoes. In: Poland, M.P., Takahashi, T.J., Landowski, C.M. (Eds.) *Characteristics of Hawaiian volcanoes*, USGS Professional Paper 1801. US Geological Survey, Reston, VA, 237–292. <https://doi.org/10.3133/pp18016>

Helz, R.T., Clague, D.A., Mastin, L.G., Rose, T.R. (2015) Evidence for Large Compositional Ranges in Coeval Melts Erupted from Kilauea's Summit Reservoir. In: Carey, R., Cayol, V., Poland, M., Weis, D. (Eds.) *Hawaiian Volcanoes: From Source to Surface*. American Geophysical Union and Wiley, Hoboken, NJ, 125–145. <https://doi.org/10.1002/9781118872079.ch7>

Helz, R.T., Cottrell, E., Bounce, M.N., Kelley, K.A. (2017) Olivine-melt relationships and syneruptive redox variations in the 1959 eruption of Kīlauea Volcano as revealed by XANES. *Journal of Volcanology and Geothermal Research* 333–334, 1–14. <https://doi.org/10.1016/j.jvolgeores.2016.12.006>

Iacono-Marziano, G., Morizet, Y., Le Trong, E., Gaillard, F. (2012) New experimental data and semi-empirical parameterization of H₂O–CO₂ solubility in mafic melts. *Geochimica et Cosmochimica Acta* 97, 1–23. <https://doi.org/10.1016/j.gca.2012.08.035>

Jarosewich, E., Nelen, J.A., Norberg, J.A. (1980) Reference Samples for Electron Microprobe Analysis. *Geostandards Newsletter* 4, 43–47. <https://doi.org/10.1111/j.1751-908X.1980.tb00273.x>

Lamadrid, H.M., Moore, L.R., Moncada, D., Rimstidt, J.D., Burruss, R.C., Bodnar, R.J. (2017) Reassessment of the Raman CO₂ densimeter. *Chemical Geology* 450, 210–222. <https://doi.org/10.1016/j.chemgeo.2016.12.034>



Lerner, A.H., Wallace, P.J., Shea, T., Mourey, A.J., Kelly, P.J., Nadeau, P.A., Elias, T., Kern, C., Clor, L.E., Gansecki, C., Lee, R.L., Moore, L.R., Werner, C.A. (2021) The petrologic and degassing behavior of sulfur and other magmatic volatiles from the 2018 eruption of Kīlauea, Hawai‘i: melt concentrations, magma storage depths, and magma recycling. *Bulletin of Volcanology* 83, 43. <https://doi.org/10.1007/s00445-021-01459-y>

Lin, F., Bodnar, R.J., Becker, S.P. (2007) Experimental determination of the Raman CH₄ symmetric stretching (ν_1) band position from 1–650 bar and 0.3–22 °C: Application to fluid inclusion studies. *Geochimica et Cosmochimica Acta* 71, 3746–3756. <https://doi.org/10.1016/j.gca.2007.05.016>

Matzen, A.K., Baker, M.B., Beckett, J.R., Stolper, E.M. (2011) Fe–Mg Partitioning between Olivine and High-magnesian Melts and the Nature of Hawaiian Parental Liquids. *Journal of Petrology* 52, 1243–1263. <https://doi.org/10.1093/petrology/egg089>

Montierth, C., Johnston, A.D., Cashman, K.V. (1995) An Empirical Glass-Composition-Based Geothermometer for Mauna Loa Lavas. In: Rhodes, J.M., Lockwood, J.P. (Eds.) *Mauna Loa Revealed: Structure, Composition, History, and Hazards*, Geophysical Monograph Series 92, American Geophysical Union, Washington, D.C., 207–217. <https://doi.org/10.1029/GM092p0207>

Moussallam, Y., Edmonds, M., Scaillet, B., Peters, N., Gennaro, E., Sides, I., Oppenheimer, C. (2016) The impact of degassing on the oxidation state of basaltic magmas: A case study of Kīlauea volcano. *Earth and Planetary Science Letters* 450, 317–325. <https://doi.org/10.1016/j.epsl.2016.06.031>

Newman, S., Lowenstern, J.B. (2002) VOLATILECALC: a silicate melt–H₂O–CO₂ solution model written in Visual Basic for excel. *Computers & Geosciences* 28, 597–604. [https://doi.org/10.1016/S0098-3004\(01\)00081-4](https://doi.org/10.1016/S0098-3004(01)00081-4)

Ryan, M.P. (1987) Elasticity and contractancy of Hawaiian olivine tholeiite and its role in the stability and structural evolution of sub-caldera magma reservoirs and rift systems. In: Decker, R.W., Wright, T.L., Stauffer, P.H. (Eds.) *Volcanism in Hawaii*, USGS Professional Paper 1350. US Geological Survey, Reston, VA, 1395–1447. https://pubs.usgs.gov/pp/1987/1350/pdf/chapters/pp1350_ch52.pdf

Schindelin, J., Arganda-Carreras, I., Frise, E., Kaynig, V., Longair, M., Pietzsch, T., Preibisch, S., Rueden, C., Saalfeld, S., Schmid, B., Tinevez, J.-Y., White, D.J., Hartenstein, V., Eliceiri, K., Tomancak, P., Cardona, A. (2012) Fiji: an open-source platform for biological-image analysis. *Nature Methods* 9, 676–682. <https://doi.org/10.1038/nmeth.2019>

Shea, T., Matzen, A.K., Mourey, A.J. (2022) Experimental study of Fe–Mg partitioning and zoning during rapid growth of olivine in Hawaiian tholeiites. *Contributions to Mineralogy and Petrology* 177, 114. <https://doi.org/10.1007/s00410-022-01969-8>

Shishkina, T.A., Botcharnikov, R.E., Holtz, F., Almeev, R.R., Jazwa, A.M., Jakubiak, A.A. (2014) Compositional and pressure effects on the solubility of H₂O and CO₂ in mafic melts. *Chemical Geology* 388, 112–129. <https://doi.org/10.1016/j.chemgeo.2014.09.001>

Sides, I., Edmonds, M., MacLennan, J., Houghton, B.F., Swanson, D.A., Steele-MacInnis, M.J. (2014a) Magma mixing and high fountaining during the 1959 Kīlauea Iki eruption, Hawai‘i. *Earth and Planetary Science Letters* 400, 102–112. <https://doi.org/10.1016/j.epsl.2014.05.024>

Sides, I.R., Edmonds, M., MacLennan, J., Swanson, D.A., Houghton, B.F. (2014b) Eruption style at Kīlauea Volcano in Hawai‘i linked to primary melt composition. *Nature Geoscience* 7, 464–469. <https://doi.org/10.1038/ngeo2140>



Span, R., Wagner, W. (1996) A New Equation of State for Carbon Dioxide Covering the Fluid Region from the Triple-Point Temperature to 1100 K at Pressures up to 800 MPa. *Journal of Physical and Chemical Reference Data* 25, 1509–1596. <https://doi.org/10.1063/1.555991>

Steele-MacInnis, M., Esposito, R., Moore, L.R., Hartley, M.E. (2017) Heterogeneously entrapped, vapor-rich melt inclusions record pre-eruptive magmatic volatile contents. *Contributions to Mineralogy and Petrology* 172, 18. <https://doi.org/10.1007/s00410-017-1343-3>

Wang, X., Chou, I.-M., Hu, W., Burruss, R.C., Sun, Q., Song, Y. (2011) Raman spectroscopic measurements of CO₂ density: Experimental calibration with high-pressure optical cell (HPOC) and fused silica capillary capsule (FSCC) with application to fluid inclusion observations. *Geochimica et Cosmochimica Acta* 75, 4080–4093. <https://doi.org/10.1016/j.gca.2011.04.028>

Wieser, P.E., DeVitre, C.L. (2023) DiadFit: An Open-Source Python3 Tool for Peak fitting of Raman Data from silicate melts and CO₂ fluids. *EarthArXiv*. <https://doi.org/10.31223/X5CQ1F>

Wieser, P.E., Edmonds, M., Maclennan, J., Jenner, F.E., Kunz, B.E. (2019) Crystal scavenging from mush piles recorded by melt inclusions. *Nature Communications* 10, 5797. <https://doi.org/10.1038/s41467-019-13518-2>

Wieser, P.E., Lamadrid, H., Maclennan, J., Edmonds, M., Matthews, S., Iacovino, K., Jenner, F.E., Gansecki, C., Trusdell, F., Lee, R.L., Ilyinskaya, E. (2021) Reconstructing Magma Storage Depths for the 2018 Kīlauean Eruption From Melt Inclusion CO₂ Contents: The Importance of Vapor Bubbles. *Geochemistry, Geophysics, Geosystems* 22, e2020GC009364. <https://doi.org/10.1029/2020GC009364>

Yuan, X., Mayanovic, R.A. (2017) An Empirical Study on Raman Peak Fitting and Its Application to Raman Quantitative Research. *Applied Spectroscopy* 71, 2325–2338. <https://doi.org/10.1177/0003702817721527>